One-Pot Synthesis of Luminescent and Photothermal Carbon Boron-Nitride Quantum Dots Exhibiting Cell Damage Protective Effects

Grazia M. L. Consoli[a,b], Ludovica Maugeri[c], Nicolò Musso[d], Antonino Gulino[e], Luisa D'Urso[e], Paolo Bonacci[d], Gianpiero Buscarino[f], Giuseppe Forte[c] and Salvatore Petralia** [a,b,c,g]

[a]*CNR-Institute of Biomolecular Chemistry, Via Paolo Gaifami 18, 95126 Catania, Italy*

[b]*CIB-Interuniversity Consortium for Biotechnologies U.O. of Catania, Via Flavia, 23/1, 34148 Trieste, Italy*

[c]*Department of Drug and Health Sciences, University of Catania, Via Santa Sofia 64, 95125 Catania, Italy*

[d]*Department of Biomedical and Biotechnological Sciences, University of Catania, Via S. Sofia 97, Catania, Italy*

[e]*Department of Chemical Science, University of Catania, and I.N.S.T.M. UdR of Catania, Via Santa Sofia 64, 95125 Catania, Italy*

[f]*Department of Physic and Chemistry, University of Palermo, Via Archirafi 36, Palermo, Italy*

[g]*NANOMED, Research Centre for Nanomedicine and Pharmaceutical Nanotechnology, University of Catania, Viale A. Doria 6, 95124 Catania, Italy*

KEYWORDS: nanomaterials, luminescent boron nitride quantum-dots, photothermal, antioxidant, anti-inflammatory effect

ABSTRACT

Zero-dimensional boron nitride quantum dots (BNQDs) are arousing interest for their versatile optical, chemical, and biochemical properties. Introducing carbon contents in BNQDs nanostructures is a great challenge to modulate their physic-chemical properties and applications. Among the carbon

moieties, phenolic groups have attracted attention for their biochemical properties and phenol-containing nanomaterials are showing great promise for biomedical applications. Herein, the first example of direct synthesis of water dispersible BNQDs exposing phenolic and carboxylic groups is presented. The carbon-BNQDs were prepared in a single step by solvent-assisted reaction of urea with boronic reagents and were characterized by optical absorption and luminescence techniques, Raman, FTIR and NMR spectroscopy, XPS, DLS, and AFM microscopy. The carbon-BNQDs exhibited nano-dimension, high photothermal conversion efficiency, pH-responsive luminescence and Z-potential, and good stability. The potential of the carbon-BNQDs to provide photothermal materials also in solid state by embedding in agarose substrate was successfully investigated. The carbon-BNQDs exhibited biocompatibility on colorectal adenocarcinoma cells (Caco-2) and protective effects from chemical and oxidative stress on Caco-2, osteosarcoma (MG-63) and microglial (HMC-3) cells. Amplicon mRNA-seq analyses for the expression of 56 genes involved in oxidative stress and inflammation were performed to evaluate the molecular events responsible for the cell protective effects of the carbon-BNQDs.

1. Introduction

Quantum dots (QDs) represent an interesting class of low-dimensional nanomaterials recently rewards by Nobel Prize in Chemistry 2023. These nanosized materials offering significant advantages due to their large surface area, diverse surface chemistry, controllable structures, and unique optical and physical properties have aroused and continue to attract a wide interest holding great promise in a huge of applications [1,2,3] A variety of metal-,[4] metal oxide-[5], graphene-[6], boron nitride-[7], and carbon-based nanostructures[8] with extraordinary chemical and physical properties have been produced. Among them, photothermal nanostructures, able to convert absorbed light into heat, are receiving increasing attention for biomedical applications including enzymatic activity induction,[9] photo-induced hyperthermia disease treatment, [10] and combined chemo-photothermal therapy.[11,12] Moving from two-dimensional to zero-dimensional nanostructures is opening up novel research areas due to the emergence of unique optical and physicochemical properties, excellent thermal and chemical stability, and desirable biocompatibility. The layered structure of boron nitride has been exploited to form different nanostructures such as nanotubes, nanosheets and quantum dots (QDs). Boron nitride quantum dots (BNQDs) are an interesting class of zero-dimensional materials with intense absorbance and high photothermal conversion yield, versatile fluorescent, optoelectronic, chemical, biochemical, and photothermal properties. [13,14,15] BNQDs exhibited higher

photophysical, chemical and photochemical stability than metal quantum dots and more biocompatibility than carbon quantum dots. [16,17]

Post-synthesis functionalization is a tested strategy to modulate chemical and electronic properties of various quantum dots including graphene-QDs,[18] silicene-QDs[19] and silicon-carbide-QDs. [20] Particular properties may also emerge from the smart chemical functionalization of BNQDs at the surface and edge region. Due to the very small dimension, in BNDQs the amount of dangling bonds at the edge atoms (boron and nitrogen) in relation to the saturated sp^2 bonds on the surface is very high. This allows for an effective chemical edge-functionalization by introducing valid functional groups to properly tune optical, electronic, physical, and chemical properties.[21,22] Many efforts have been made to change the surface/edge chemistry of BNQDs and derivatives with applications ranging from electronics to medicine have been produced.[13,21,22] Recently, Tao *et al* proposed an interesting approach to prepare thermostable and full color-BNQDs, through the functionalization of the BNQD edge atoms with different amino-based molecules. The resulting BNQD derivatives showed a photoluminescence at a long-wavelength region (420-610 nm) and high fluorescence yield.[23]

The integration of natural organic molecules, such as phenols, in nanostructured materials has inspired the development of new and highly efficient hybrid nanomaterials for biomedical applications. Recent literature has widely reported that phenolic and polyphenolic compounds have strong protective effect against cell damage,[24] cancer prevention,[26] anti-inflammatory,[30] and antibacterial[27] activities. These properties are mainly related to antioxidant effects. Indeed, ongoing research has indicated that phenolic compounds enhance cells' antioxidant capacity by stimulating the expression of enzymes involved in oxygen metabolism and xenobiotic detoxification,[28] reduce the levels of cellular ROS by scavenging them directly or inhibiting their production,[29] and suppress multiple signalling pathways linked to inflammatory reactions on pollutant-exposed cells.[30] As antibacterials, phenolic compounds can target multiple sites (membrane, DNA, enzyme) in bacteria, leading to a much higher cell sensitivity. Recently, polyphenol-containing nanostructured materials have been explored for application as pro-drug [31,32] and new agents for chemodynamic therapy,[33] photothermal therapy,[34], gene therapy,[35] and bioimaging. [36]

Very few papers concern phenol-containing boron nitride nanostructured materials. As an example, very recently, Kin and coworker developed a novel deposition method to prepare nanocomposites based on boron nitride nanotubes containing plant-based polyphenols for polymer technology application.[37] To the best of our knowledge, literature reports on carbon-containing BNQDs prepared

by post-synthesis functionalization, but nothing has yet been reported on the direct synthesis of carbon-BNQDs.

Inspired by the above considerations, herein we report the first example of direct synthesis of multifunctionalized carbon-BNDQs (scheme 1A). The proposed unprecedented one-pot chemical procedure provides water dispersible, luminescent and photothermal BNDQs exposing phenolic and carboxylic groups on the edge atoms. The carbon-BNQDs were characterized for structure and optical properties using different techniques including optical absorption and emission spectroscopy, Raman, FTIR, and NMR spectroscopy, Dynamic Light scattering, Z-potential, cyclic voltammetry, X-ray Photoelectron Spectroscopy (XPS), and Atomic Force Microscopy (AFM). Moreover, green light-induced photothermal effects of the carbon-BNDQs in water dispersion or embedded on solid substrate were demonstrated and the photothermal conversion yield efficiency measured. Biocompatibility and cell protection effects from chemical damage and oxidative stress of the carbon containing BNDQs, were also demonstrated. Finally, to explore the molecular mechanisms responsible for the beneficial effect of the carbon-BNQDs, mRNA-seq experiments were performed to evaluate the expression of 56 genes involved in oxidative stress, apoptosis, and cell metabolism (scheme 1-B).

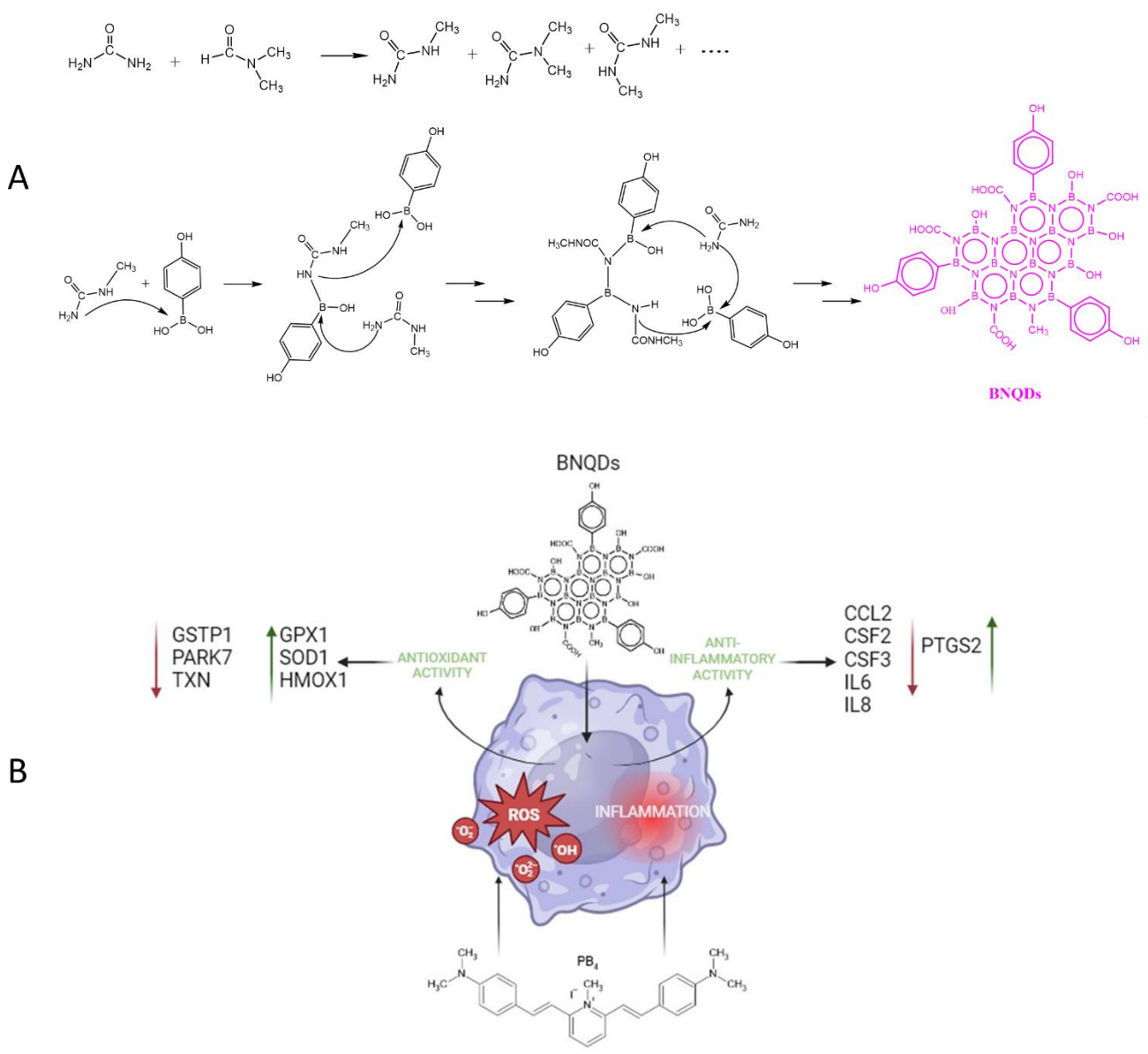

Scheme 1. Carbon-BNQDs: A) synthetic route for preparation and schematic representation of their hypothesized structure; B) Schematic representation of the more significant RNA expression modifications involved in the carbon-BNQDs cell protective effect from toxic eteroaryl-ethilene (PB4) insult.

2. Results and Discussion

2.1 . Synthetic strategy and structure of the carbon-BNQDs.

Water-dispersible carbon-BNQDs were prepared by a one-pot chemical approach from urea and 4-hydroxyphenylboronic acid in dimethylformamide (DMF) solvent, as depicted in scheme 1-A. The condensation reaction occurs through a solvent-assisted mechanism. Firstly, urea is converted to *N*-methyl-derivatives by reaction with DMF, then the neo-formed *N*-methyl-urea derivatives react with the boron precursor to produce the first six-member ring BN nanostructure that by multiple condensation reactions provides the carbon-BNQDs structures. The changes of the optical absorption spectrum during the BNQDs synthesis at variour reaction time (1, 4, 6, and 9 hrs) showed the appearance of absorption bands in the region 220-700 nm, indicative of an efficient carbon derivatization of the BN nanostructures (Figure S1). The proposed solvent-assisted mechanism (Scheme 1-A) was corroborated by performing the synthesis in a methyl-free solvent (tetrahydrofuran, THF). In this case, slight optical absorption changes were observed after 9 hrs of reaction to indicate that in the absence of methyl-donor solvent the reaction does not occur or takes place very slowly (Figure S2).

The optical properties of the BNQDs were investigated by absorption and emission spectroscopies, as illustrated in Figures 1A and 1B. In details, the optical absorption spectra in water show typical $\pi\pi^*$ absorption bands in the range from 250 nm to 400 nm. An additional low and broad absorption band is observed around 500-550 nm. As expected for nanostructured materials, the emission fluorescence spectra at various excitation wavelength (360, 380, 400, 420, 440, 460, 480, 500, and 520 nm) showed a typical excitation-dependent emission with a maximum emission peak at about 480 nm.

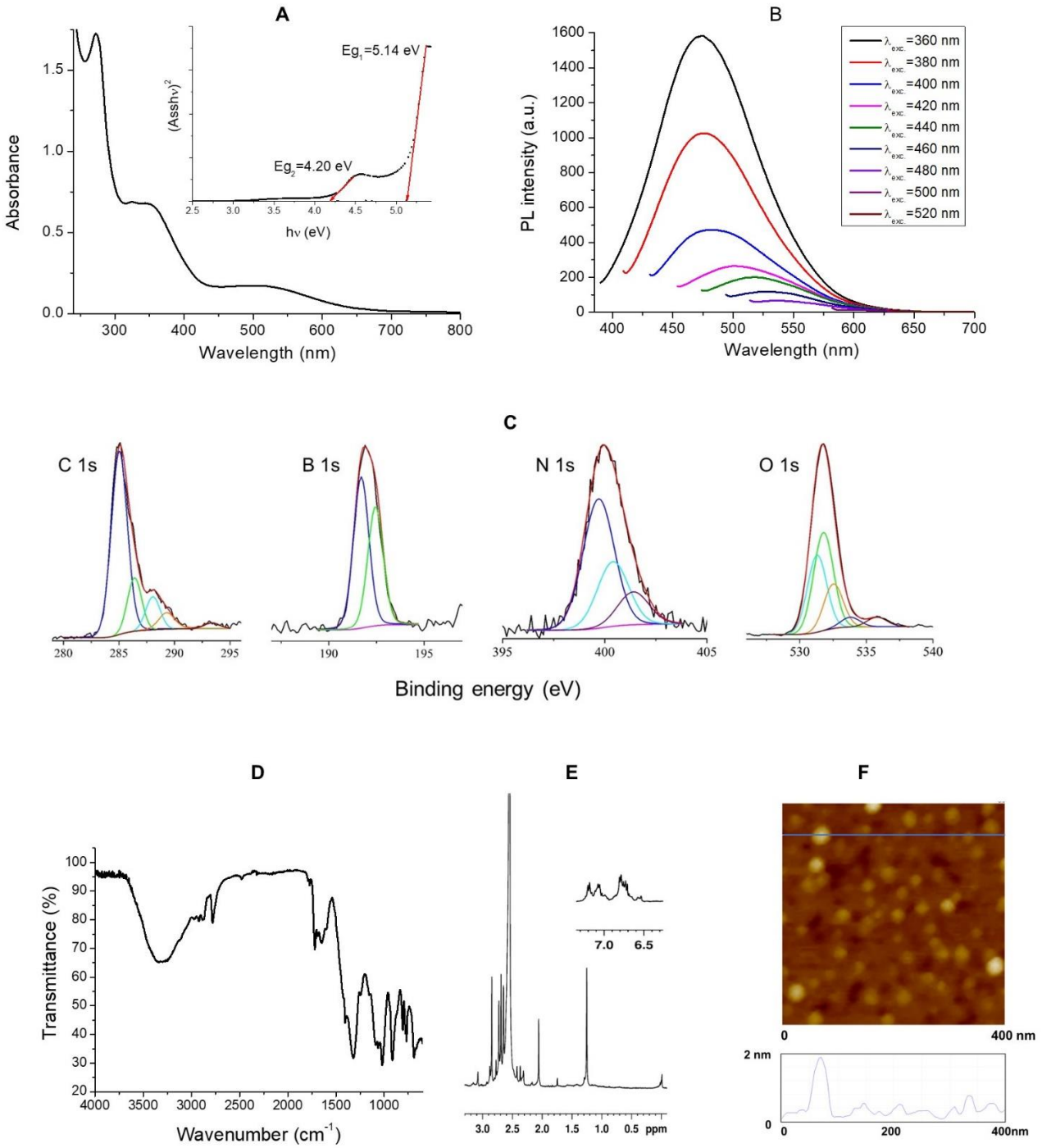

Figure 1. BNQDs dispersed in water: A) optical absorption spectrum (inset: the indirect optical band gap calculation); B) emission fluorescence spectra at various excitation wavelength (360, 380, 400, 420, 440, 460, 480, 500, and 520 nm); C) Al Kα excited XPS in: C1s, B1s, N1s, and O1s energy region; D) FTIR-ATR spectra; E) methyl region of the ^{1}H NMR spectrum (inset: aromatic region); F) representative AFM images obtained on MICA substrate: full scan analysis, 400×400 nm, and cross sections.

To confirm the presence of phenolic moieties in the BNQDs, urea and boric acid (H_3BO_3) were subjected to the same one-pot procedure. The obtained bare-BN sheets exhibited the typical BN sharp absorption band at about 216 nm but no absorption above 240 nm (Figure S3). For a further comparison, the optical band gap energy (E_g) of the carbon-BNQDs and bare-BN were determined from the absorption spectra using the Tauc's equation $(Ass\ h\upsilon)^n = K(h\upsilon - E_g)$, where Ass is the absorbance coefficient, h is the Planck's constant, ν is the frequency, E_g is the optical energy gap and n is the constant associated to the different types of electronic transitions. According to the UV-Vis absorption spectra and literature data, reporting for BN nanostructures an indirect allowed transition (n = 2), an indirect optical band gap around E_{g1}= 5.56 eV was estimated for the bare-BN. This value agreed with the energy gap value reported in literature for exfoliated BN nanosheets (Figure S3, inset).[38] Lower band gap values of E_{g1}= 5.14 eV (inset Figure 1A) estimated for the BNQDs were indicative of an effective BN carbon-functionalization. A gradually decrease of the optical band gap by increasing the carbon content is reported in literature for exfoliated BN nanostructures.[39,40] Additionally, the optical band gap at about E_{g2}= 4.2 eV is reasonably ascribable to carbon-substituted BNQDs as reported in literature[41,42] and recently by Thamankar *et al*.[43] In summary, the red-shifted optical absorption bands above 350 nm observed for the BNQDs in comparison with the bare-BNs, undoubtedly supported the formation of carbon-functionalized BNQDs structures.

The electronic structure of the carbon-BNQDs was investigated by X-ray photoelectron spectroscopy. This technique is ideal as it gives information on the oxidation states and chemical environment of the studied species and allows estimation of the surface elemental composition once the relevant atomic sensitivity factors have been considered.[44-48] Figure 1C shows the high-resolution XP spectrum of the functionalized carbon-BNQDs in C1s, B1s, N1s, and O1s energy region. In particular, in the C 1s binding energy region, the fitting of the spectrum required five Gaussian components centred at 285.0, 286.3, 288.0, 289.4, and 293.3 eV. The black line refers to the experimental profile, the magenta line refers to the background while the red line, superimposed to the experimental profile, refers to the sum of the Gaussian components. The first component at 285.0 eV (blue line) is due to the C=C/C-C bonds of the phenolic terminations, together with some adventitious carbons omnipresent on air-exposed materials. The components centred at 286.3 eV (green line) and 288.0 eV (cyan line) are assigned to the phenolic C-B (Figure 3) and amide (O=C-NH) species, respectively.[44,45] Note that, the C-B bond in the BNQDs refers to a phenolic carbon bonded to the six-member ring BN structure, and sensibly differs from that of the boron carbide that should lie at about 282.3 eV. The peak at 289.4 eV (orange line) is due to the carboxylic acid (-COOH) groups.[49] These last three components (286.3, 288.0, 289.4 eV) show relative intensity ratios close to 3:2:1, thus indicating

the phenolic C-B as the most intense carbon state, within the phenolic C-B, O=C-NH and -COOH groups. This result is not unexpected since the boronic starting material for the preparation of the BNQDs is functionalized with phenols. Finally, the peak centred at 293.3 eV (magenta line) is ascribed to the $\pi \rightarrow \pi^*$ shake-up satellite, due to the presence of the aromatic phenolic groups.[44] The red line, superimposed to the experimental profile, refers to the sum of the Gaussian components. In the B 1s binding energy region, the deconvolution of the spectrum required two Gaussian components having an intensity ratio of 1.2:1 and centred at 191.6 eV (blue line) and 192.4 eV (green line). The Gaussian component centred at lower binding energy (191.6 eV) is due to the B-N states, while the Gaussian component at 192.4 eV is assigned to the N-B-C states of the phenol functionalized BNQDs.[50-52] The magenta line refers to the background, while the red line, superimposed to the experimental profile, refers to the sum of the Gaussian components. In the N 1s binding energy region a careful fitting of the experimental profile of this N 1s signal required three Gaussian components centred at 399.7 eV (blue line), 400.5 eV (cyan line), and 401.4 eV (purple line). The peak at a lower binding energy value (399.7 eV) is ascribed to the aromatic B-N levels.[50,52] The component centred at 400.5 eV is assigned to the amide (O=C-NH) species.[53-54] Finally, the peak at a higher binding energy value (401.4 eV) is due to some quaternized nitrogen.[55] These three components show relative intensity ratios close to 4:2:1, thus indicating the B-N as the most intense nitrogen state. The magenta line refers to the background, while the red line, superimposed to the experimental profile, refers to the sum of the Gaussian components. Similarly the O 1s spectral profile was fitted using five Gaussian components centred at 531.3 eV (cyan line), 531.7 eV (green line), 532.5 (orange line), 534.0 (blue line), and 536.0 eV (purple line).[56] The first component (531.3 eV) is due to the amide (O=C-NH) species; the second component, centred at 531.7 eV, is ascribed to the phenolic C-OH group; the Gaussian components at 532.5 and 534.0 eV, are safety assigned to the carboxylic (-COOH) and B-O groups.[45] Finally, the peak at higher binding energy value (536.0 eV) is due to some water molecules present on the surface of the sample. The first three components (531.3, 531.7, 532.5 eV) show intensity ratios 2:3:1, almost identical to those previously observed for the related carbon components. The difference is due to the different binding energy ordering of the oxygen components with respect to the carbon components. The magenta line refers to the background, while the red line, superimposed to the experimental profile, refers to the sum of the Gaussian components. The XPS atomic concentration analysis of the investigated systems clearly showed a ratio N/B of 1.0 with a C atomic concentration of about 50 ± 1 %. This result is in line with the phenolic functionalization of the investigated BN materials (Table S1).

FTIR-ATR investigation of carbon-BNQDs and bare-BN was also performed. FTIR-ATR peaks were observed for BNQDs at 1320 cm^{-1} and 770 cm^{-1} corresponding to B-N stretching and bending mode, respectively. The broad and intense peak at 3300 cm^{-1} related to O-H phenolic stretch and the sharp peak 1642 cm^{-1} corresponding to C=O stretch indicated the presence of phenolic and carboxylic terminations (Figure 1D). The bare-BNs showed FTIR-ATR peaks at 1386 cm^{-1} and 775 cm^{-1} corresponding to B-N stretching and B-N bending mode, respectively. The sharp peak at 3190 cm^{-1} corresponding to BO-H stretch, indicated the presence of hydroxyl groups. No relevant peaks at around 3300 cm^{-1} confirmed the absence of phenolic terminations. The spectra of the reagents (urea and boron precursor) are also presented for comparison in Figure S4. The boron precursor showed FTIR-ATR peaks at 1341 cm^{-1} and 780 cm^{-1} corresponding to B-N stretching and B-N bending mode respectively, and peaks around 3290 cm^{-1}, 3038 cm^{-1} and 1592 cm^{-1} related to O-H phenol stretch, aromatic C-H stretch and C-C ring stretch, respectively. The characteristic peaks of urea were at 1674 cm^{-1} (C=O stretch), 1460 cm^{-1} (C-N stretch), 1590 cm^{-1} (N-H stretch), and 1145 cm^{-1} (N-H bend). Raman spectra of bare-BN showed the characteristic D band at around 1400 cm^{-1}, whereas BNQDs exhibited a comparatively weaker peak at the same pattern, in line with the high exfoliated nanosized structure of the bare-BN (Figure S5).[23]

To further confirm the presence of phenolic and *N*-methyl-amide terminations, NMR spectra were performed (Figure 1E). The aromatic region of the 1H-NMR (inset Figure 1E) and 2D-COSY NMR (Figure S6) spectra of the carbon-BNDQs showed three pairs of doublets at 6.99 and 6.64 ppm, 7.04 and 6.66 ppm, 7.12 and 6.73 ppm (J = 8 *Hz*) related to phenol groups in different chemical environment. Singlets at 2.47, 2.57, 2.61, 2.65, 2.77 ppm indicated the presence of *N*-CH_3 groups (Figure 1E). Undoubtedly, these latter derived from the urea methylation occurring in DMF at 200 °C (Figure S7). It is known that DMF can react as either an electrophilic or a nucleophilic agent and can be a source of intermediates, including N-$(CH_3)_2$, CON-$(CH_3)_2$, and CH_3.[57] As a confirmation no N-CH_3 resonance was observed when the reaction of urea and 4-hydroxyphenyl boric acid was performed in THF (Figure S8). NMR spectra also supported the mechanism proposed in scheme 1 for the formation of the carbon-BNQDs (Figure S9). The proton spectrum of the BNQDs formed by heating at 200 ^{0}C for 3 hrs showed the presence of starting material (pair of doublets at 7.48 and 6.71 ppm for the phenolic protons) and new pairs of doublets (7.1 and 6.77 ppm and 6.69 and 6.64 ppm) for the phenolic groups in the forming BNQDs structures. Increasing the reaction time from 3 to 6 and 9 hrs the reagent signals disappear and the signals of the phenolic groups in BNQDs increase. At 6 hrs reaction time the boronic reagent is completely converted to the final carbon-BNQDs.

Atomic force microscopy (AFM) measurements of the carbon-BNQDs deposited on MICA substrate showed clearly recognizable QDs structures (Figure 1F). To obtain a reliable quantitative dimensional estimation of the BNQDs a statistical analysis of their diameters was performed. The diameters of the single BNQDs structures were estimated by evaluating the height from the extracted profile. As shown, the size of the BNQDs fall in the range 1-3 nm. The size distribution obtained for carbon-BNQDs is reported in Figure S10. In Figures 1F is reported a representative cross section of the carbon-BNQDs with size about 1.8 nm. DLS measurements performed for a carbon-BNQDs aqueous dispersion at pH 7.4 evidenced the presence of nanostructures with mean hydrodynamic diameter of 66.3 ± 15 nm and larger aggregates sized 245.5 ± 55.0 nm. The Z-potential value was -19.1 ± 3.9 mV. The DLS dimensional analyses confirmed the tendency of the carbon-BNQDs to form large aggregates and agreed with the band at around 500 nm observed in the experimental optical absorption spectrum (Figure 1B) and the absence of the same band in the spectrum simulated for not aggregated BNDQs as reported in the later section.

The electrochemical behaviour of the carbon-BNQDs was investigated by cyclic voltammetry (CV). As reported in literature, the oxidation of *para*-substituted phenol is reversible, pH dependent, and occurring in one oxidation step (Scheme S1). Moreover, the oxidation potential of *para*-substituted phenols varies slightly due to the *para*-substituent group.[44] The cyclic voltammograms showed the reversible oxidation-reduction process for the boron-precursor. The oxidation peak at Ec = + 0.32 V was attributed to the oxidation to catechol-quinone species while the anodic peak at Ea = - 0.41 V confirmed the reversible oxidation/reduction process. Similarly, the CV graph for the carbon-BNQDs showed the oxidation peak at Ep = + 0.45 V and the reduction peak at Ea = - 0.51 V (Figure S11).

The electrochemical behaviour of the carbon-BNQDs was also studied at different pH values. Cyclic voltammograms for BNQDs dispersion in 0.1M KCl showed Ea and Ep peaks decreasing linearly with the pH of the supporting electrolyte (Figure S12). The slope of the linear regression was about 40.5 mV per pH unit to indicate the correlation between the number of protons transferred during the phenol oxidation and the number of electrons (Figure S13).[58] The electrochemical data confirmed again the presence of phenolic terminations in the carbon-BNQD structures.

Our finding agrees with literature data reporting that optical and electronic properties of BNQDs are largely influenced by chemical functionalization, crystal structure and size. Hydroxyl, alkoxy, amino and other functional groups have been covalently attached to the electrophilic B sites of BNs nanostructures. Generally, the BNs chemical functionalization is accomplished by decreasing the HOMO-LUMO band gap.[59]

Similarly, the optical properties of BN species are influenced by crystal structure, in particular the optical band gap decreases from h-BN to rhombohedral-BN to nanotubes-BN structures [60].

2.2. pH-dependent properties of the carbon-BNQDs

To investigate the pH-responsive properties of the carbon-BNQDs, molecular modelling calculation, emission spectroscopic measurements, and Z-potential analysis were performed at different pH values (Figure 2A-E).

To this aim, molecular modelling was performed for the carbon-BNQD structures with different deprotonation degree. In particular, the following structures were investigated (Figure 2A): BNQDs-H with protonated carboxylic and phenolic residues (pH < 4.0), BNDQs-OH with deprotonated carboxylic and protonated phenolic groups (pH 7.0), and $BNDQs^-$ with deprotonated carboxylic and phenolic terminations (pH > 10). In Figure 2A are depicted the simulated absorption spectra for the three investigated structures, whereas the calculated wavelengths and the main contributions to the transitions are listed in the table depicted in Figure 2A (inset).

The modelling investigation clearly showed that only deprotonated structures ($BNQDs^-$) exhibit appreciable optical absorptions above 320 nm. In particular, the HOMO-2 →LUMO+2 electronic transition observed at 333 nm for the $BNQD^-$ mainly involves one phenate termination (which represents the HOMO-2 MO) and the $-CO-NH_2$ termination (that mainly constitutes the LUMO+2 MO), as shown in Figure 2B. The observed absorption bands are mostly due to π-π* transitions. The strongest absorption range was obtained in the range 210-225 nm, with a weaker second absorption observed around 255-260 nm for both neutral (BNQDs-H) and partially deprotonated (BNQDs-OH) structures. However, more intense, red-shifted peaks just below 300 nm were observed for the fully deprotonated structures ($BNQDs^-$) in agreement with the experimental absorption spectra. A comparison of calculated and experimental UV-vis spectra suggests that deprotonated $BNQDs^-$ are reasonably the basic structures for the described carbon-BNQDs. Notably, no strong absorption peak was observed at around 500 nm in the calculated spectra. In line with the constituent functional groups, it is plausible to hypothesize that the formation of aggregates could be responsible for the absorptions at lower energies. In Figure S14 are reported HOMO/LUMO molecular orbital shapes for the investigated structures.

Optical pH-responsive properties of the carbon-BNQDs were investigated by luminescence analysis at different pH values (from 2.5 to 12.7 range). The emission intensity of the BNQDs dispersion shifted gradually as the pH increased. This behaviour is illustrated in Figure 2C for the blue-emission

intensity (λ_{exc}= 380 nm) and in Figure 2D for the green-emission intensity (λ_{exc}= 500 nm) at different pH. Both blue- and green-emission spectra showed an increase of PL intensity as the pH increased. This behaviour is ascribable to the protonation-deprotonation process of carboxylic and phenolic groups. Moreover, the reversible protonation-deprotonation process was confirmed by fluorescence emission measurements performed upon two pH-cycles (pH 2.5, 7.4, 12.7) as reported in Figure S15. These data were corroborated by Z-potential measurements performed in the same pH range. As illustrated in Figure 2E, the Z potential value increase from -5.85 ±0.68 mV at pH 2.5 to -24.7 ± 1.7 mV as the pH increased to 12.7. In particular, at acid pH (2.5-4.5 range) both phenolic and carboxylic groups are protonated as indicated by the negligible Z-potential value (< -6 mV); in the 4.5-8.5 pH range deprotonation of the carboxylic groups can occur according to the Z-potential values (from -12 mV to -19 mV range); at higher pH (pH > 8.5) the Z-potential drastically increased to about -24 mV due to the total deprotonation of the carboxylic and phenolic groups. The stability of the BNQDs at the pH range investigated was confirmed by DLS measurements at different pH values. At pH 7.4 two main populations with hydrodynamic diameter centred at 254.5 ± 55.0 nm and 66.3 ± 15 indicated the presence of large aggregates and smaller nanostructures. The mean hydrodynamic diameter of the smaller nanostructures did not drastically change within the pH range investigated, indeed hydrodynamic size values of 95.66 ± 22.0 nm at acid condition (pH 2.5) and 82.9 ±25.1 nm at basic condition (pH 12.7) were observed.

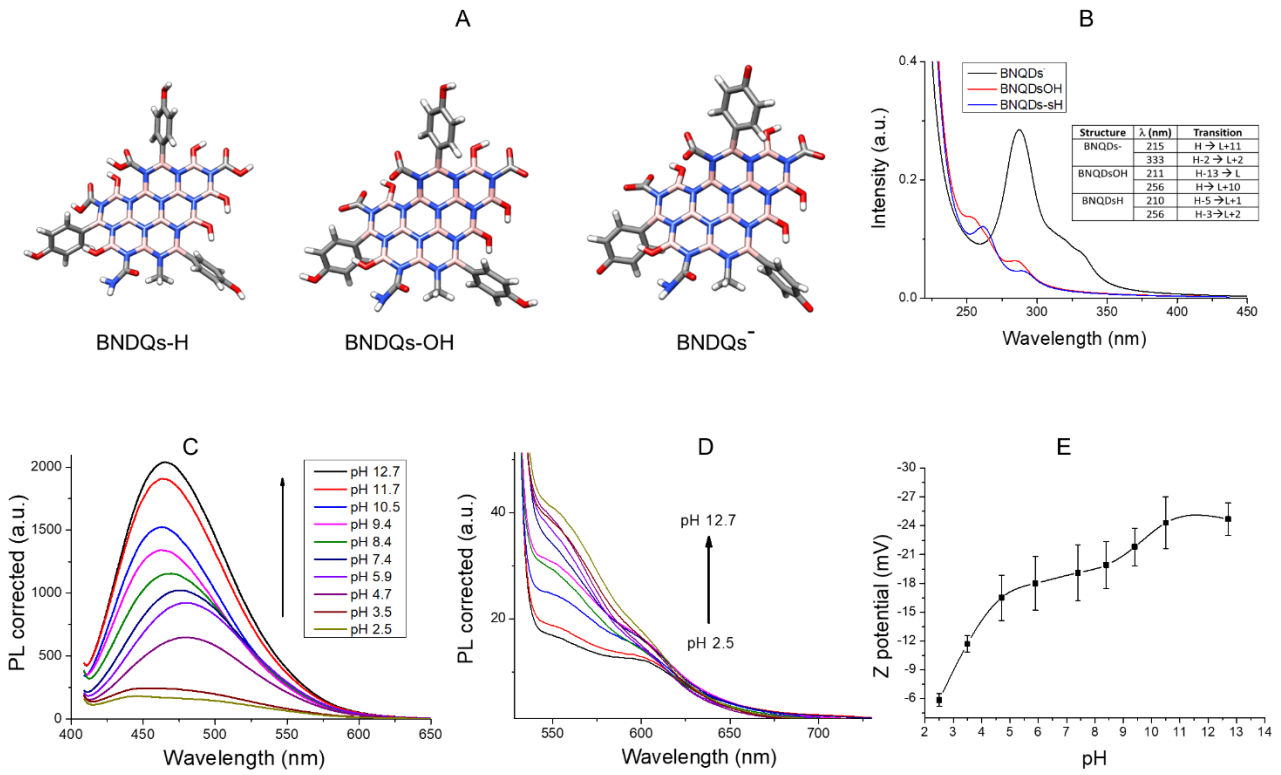

Figure 2. A) Simulated molecular structures of BNQDs with different protonation/deprotonation: BNQD-H fully protonated terminations, BNQD-OH protonated phenolic and deprotonated carboxylic terminations, and BNQD$^-$ fully deprotonated terminations; B) simulated optical absorption spectra for the three BNQD$^-$ structures at TD-CAM-B3LYP/6-31+G(d)/PCM level. The spectra are Gaussian broaded with 0.3 eV (half width half maximum). Insets the absorption wavelengths (nm) and main contributions to the transitions of simulated compounds at CAM-B3LYP/6-31+G(d)/CPM level; C-D) Fluorescence emission spectra for the BNQD water dispersion at different pH value (2.5, 3.5, 4.7, 5.9, 7.4, 8.4, 9.4, 10.5, 11.7, and 12.7) at different excitation wavelength λexc=380 nm (b) and λexc =500 nm (c); E) Z-potential measurements of the BNQD water dispersion at different pH value (2.5, 3.5, 4.7, 5.9, 7.4, 8.4, 9.4, 10.5, 11.7, and 12.7).

2.3. Photothermal properties of the carbon-BNQDs

Photothermal nanomaterials with intense light absorption are necessary to observe photothermal effects. As depicted in Figure 1A, the carbon-BNQDs show optical absorption bands around 500 nm, the absorption intensity is enough high to lead a photothermal conversion efficiency (η) that was measured by exposing various amounts of BNQDs to a laser source. In Figure 3A are reported the temperature changes, monitored by a thermo-camera, for an aqueous dispersion of BNQDs (200 µL, 1.5 mg mL^{-1}, $Abs_{532\ nm}$= 0.4 in a glass tube) and for deionized water (100 µL) as reference. The samples continuously exposed to a laser source (532 nm, power density 11.3 W cm^{-2}) reached a maximum of temperature (T_{max}). Then, the laser was turn-off and cooling cycles were recorded

(Figure 3A). The temperature increased of about 14 °C for the carbon-BNQDs sample and about 1°C for the reference (deionized water). The laser power-dependent behaviour was confirmed by experiments performed with lasers at different power density. At laser power density 0.11, 2.8, 5.5, 8.5, and 11.3 Wcm^{-2} the temperature increase was 0.5, 7.1, 13.5, 20.5, and 24.7 °C, respectively (Figure 3B).

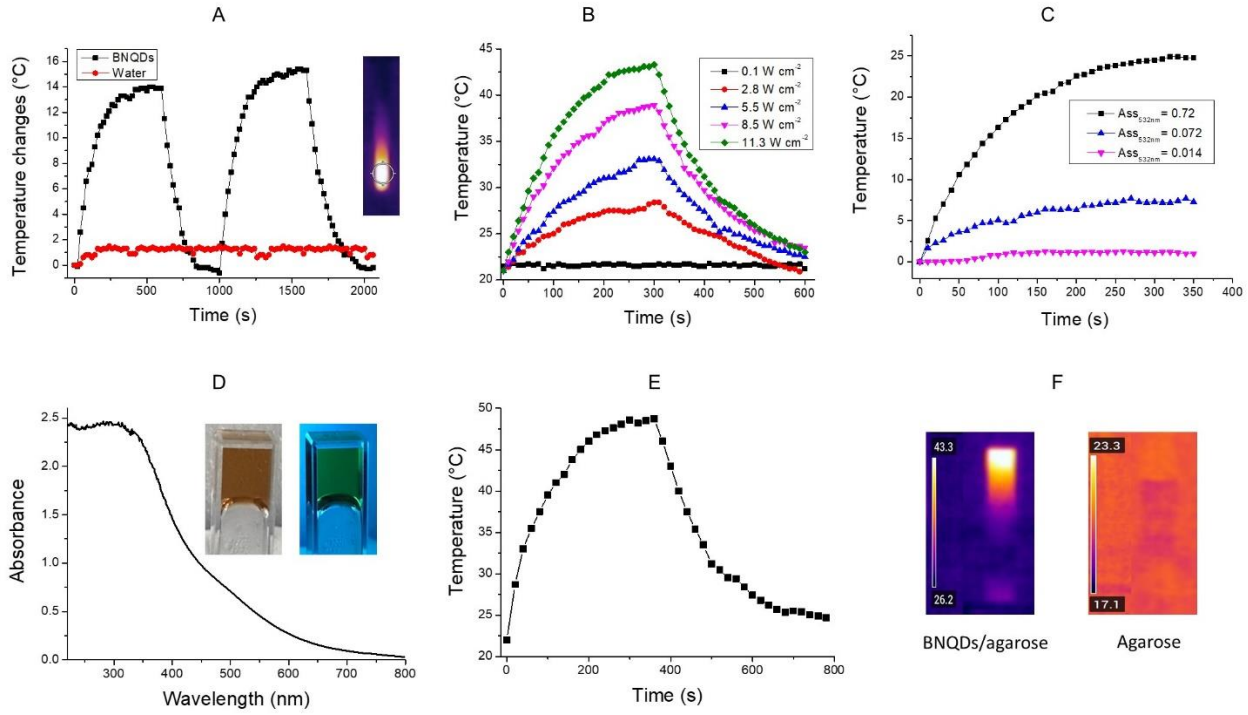

Figure 3. Photothermal experiments for BNQDs in water dispersion (1.5 mg mL^{-1}, 200 µL volume in a glass-tube): A) photothermal heating-cooling cycles (inset representative thermograph images); B) photothermal effect at different laser power density; C) photothermal experiments at different absorbance values at 532 nm (Laser 532 nm, power density 16.9 W cm^{-2}). Photothermal experiment for BNQD-agarose (0.4%): D) optical absorption spectra of BNQD-agarose (inset photographs of BNQD-agarose environment light (left) and under 254 nm UV lamp (right); E) photothermal heating-cooling cycle; D) representative thermographs of BNQD-agarose (left) and agarose (right) substrate.

To better investigate the photothermal activity of carbon-BNQDs, experiments were conducted with various amounts of nanostructures. In particular, aqueous dispersions of carbon-BNQDs with different absorbance values were sexposed to laser excitation (532 nm). The results reported in Figure 3C indicate that the temperature of the carbon-BNQDs dispersion increases with increasing absorbance. In particular, the temperature increased by about 0.1, 5.2, and 25 °C at absorbance values of 0.044, 0.072 and 0.72, respectively. Thermographs recorded by a thermo-camera during the photothermal experiments in glass tube are depicted in Figure 3A inset. The change of temperature

during cooling was monitored to confirm the rate of heat transfer of the system. The time constant (τ_s) for the carbon-BNQDs was calculated to be 139 ± 1.1 s at laser power density 8.5 Wcm^{-2} (Figure S16). This value was conformed also for the laser power density value of 11.3 Wcm^{-2} and a comparable time constant τ_s value of 133 ± 0.9 s. Based on the data, the light-driven photothermal conversion efficiency (η) of the carbon-BNQDs was calculated to be 60.7 % (Table S2).

Embedded into agarose, carbon-BNQDs could provide luminescent and photothermal substrates with flexibility and good mechanical and optical properties enabling application on biomedical engineering.[46] As a proof-of-concept, solid substrates were prepared by embedding the carbon-BNQDs into 0.4% agarose and optical and photothermal properties of the BNQDs/agarose material were investigated. The optical absorption spectra, illustrated in Figure 3D, show the typical BNQD' s absorption at wavelength above 300 nm. Inset in figure 3D, shows the photographs of the BNQDs-agarose under environment light and under 254 nm UV lamp, evidencing the green-luminescence of BNQDs. The excellent photothermal behavior of the BNQDs-agarose substrate was demonstrated by the excellent photothermal conversion yield (η= 90%) and by the time constant τ_s=44.3 s (Figure 3E, Table S3 and Figure S17). Figure 3E depicts the photothermal cycle of BNQDs-agarose upon excitation with a laser source (532 nm, power density 11.3 W cm^{-2}). The laser was turn-off and two heating and cooling cycles were recorded. Figure 3F illustrates representative thermographs of BNQDs-agarose and agarose, respectively.

2.4. Biocompatibility of the carbon-BNQDs and cell protective action assessment

To investigate the beneficial effect of the carbon-BNQDs on cells treated with toxic agents, three experiments were conducted. Firstly, the biological cell compatibility of the BNQDs at various concentration was evaluated. Next, cell viability tests on three cell lines at different incubation time (6 and 24 hours) were carried out to assess the cell protective effect of the BNQDs from chemical damage induced by eteroaryl-ethilene (PB4) and from oxidative stress induced by 5-Fluorouracil (5-Fu). Finally, amplicon mRNA-seq were performed to evaluate the molecular pathways of the BNQD's cell protective effect. RNA-seq experiments on a custom gene panel were performed to evaluate the expression variation for 56 genes, involved in oxidative stress, apoptosis and cell metabolism, in cells untreated and treated with the carbon-BNDQs before to be subjected to external toxic stimuli.

2.5. Biocompatibility experiments

To evaluate the effect of the carbon-BNQDs on cells viability, human colorectal cells (CaCo-2) were exposed to increasing concentration of BNQDs (0.004, 0.04, 0.4, and 40 μg/200 μL^{-1}) for 24 hrs and

the cell growth was compared with the one of untreated cells (CTRL) and cells treated with 5-Fluorouracil (5-FU, 100 µM) as a standard cytotoxic medication used in cancer chemotherapy. As illustrated in Figure 4A, at the end of the treatment and at any concentration used, the cell viability was comparable to that of untreated control and no remarkable effects on cell morphology were observed after exposure to BNQDs. Figure 4B report the representative photographs of untreated cells (CTRL) and cells treated with various amount of carbon-BNQDs (0.004, 0.04, 0.4, 4, and 40 µg 200µL^{-1}). These results confirmed the excellent cell biocompatibility of the carbon-BNQDs. Statistical differences values are reported in table S4.

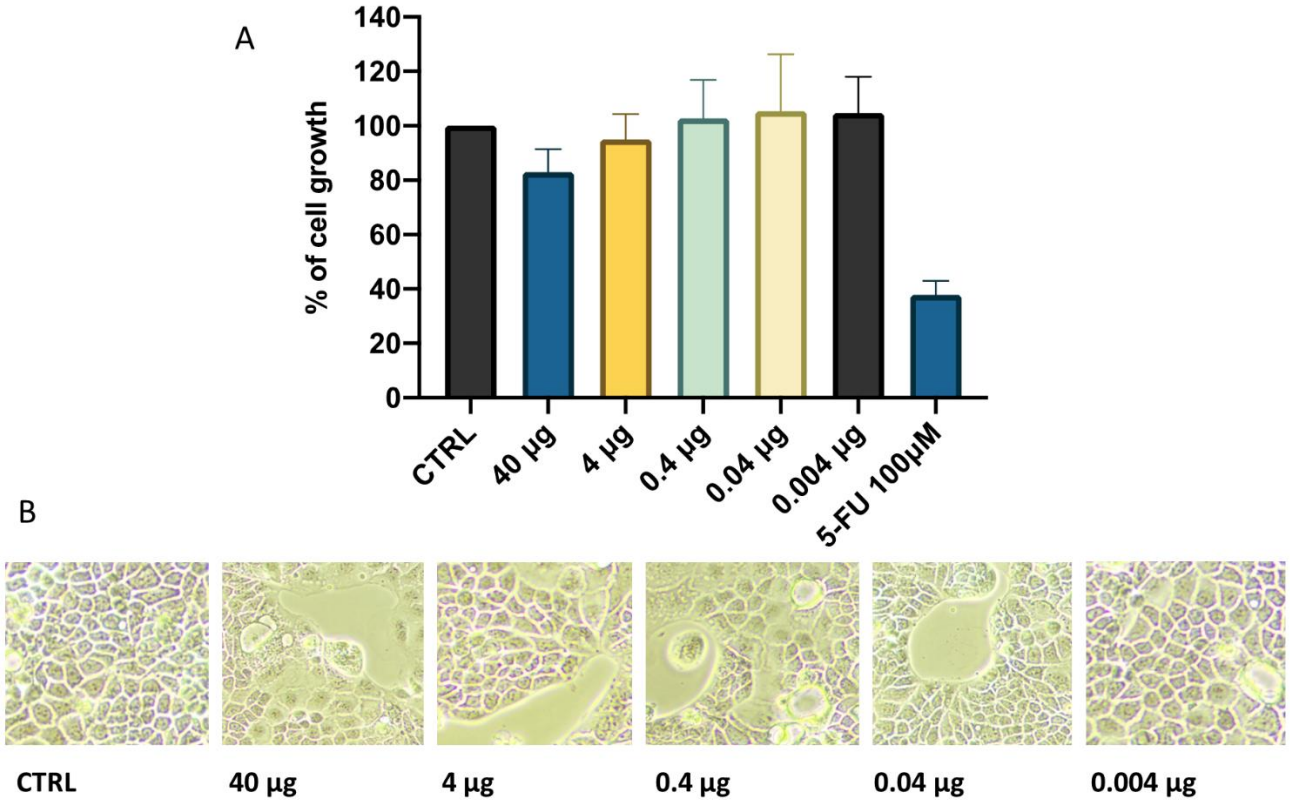

Figure 4. Cell viability experiments: A) MTT assay for Caco-2 in the presence of decreasing amounts of BNQDs (0.004, 0.04, 0.4, 4, and 40 µg 200µL^{-1}), untreated cells (CTRL) and cells treated with 5-Fu (100 µM). Percentage of treated cell growth is compared to control (CTRL) (p-values comprises from <0.0001 and 0.0002); B) representative photographs of cells untreated (CTRL) and treated with different amount of BNQDs (Inverted Microscope Nikon ECLIPSE Ts2 – FL at 40X).

2.6. Evaluation of the cell protective effect against toxic agents

To assess the cell protective effect of the carbon-BNQDs against toxic agents, cell viability experiments were performed on three different cell lines: colorectal adenocarcinoma (Caco-2),

microglial HMC-3, and osteosarcoma MG-63 cells treated with 5-Fu (100 µM) or PB4 (0.15 µM). 5-Fu is a strong anti-cancer drug largely used in colorectal cancer treatment. It can affect different cellular pathways. In particular, 5-FU can induce cytotoxicity by interacting with the mitotic S-G2 phase,[61] promotes apoptosis by up-regulation of p53 (TP53) gene, induces ROS production,[62] and increases the amount of intracellular iron with consequent ferroptosis.[63] The cytotoxic effect of 5-FU is mainly due to the inhibition of cellular thymidylate synthase leading to the prevention of DNA replication and inhibition of RNA synthesis by the integration of its metabolites into RNA.[64] All these make 5-Flu one of the most used toxic agents to induce cytotoxic effect in different cell lines. PB4 is an heteroaryl-ethylene compound developed and tested by our group. [65,66] Its cytotoxicity was confirmed by the IC50 value of about 0.3 µM. Based on its high cytotoxicity, all tests were performed using a PB4 concentration of 0.15 µM to induce an effective cell stressful without risking compromising cell viability. MTT assay results performed on the three cell lines treated with 5-Fu (100 µM) and with PB4 (0.15 µM) showed an effective and cell-line dependent protective effect after pre-treatment with the carbon-BNQDs (4 µg 200 μL^{-1}). In detail, for Caco-2 lines treated with 5-Fu, the protective effect was demonstrated by total recovery of cell viability after 6 hours, and by the increasing of cell viability from about 60% to 75 % after 24 hours. The differences are statistical in both cases (Figure 5A-5B). The MTT experiments for HMC-3 cell line treated with 5-Fu demonstrated a statistically significant difference between BNQD-treated and untreated cells (Figure 5A-5B). A net increase of cell viability from 64% (untreated cells) to 77% and 73% after 6 and 24 hours of incubation time respectively, confirmed the beneficial effect of the BNQDs for this cell line (Figures 5A-5B). Statistical difference values are reported in table S5. Slight statistical difference for MTT experiments between BNQD-treated and -untreated cells after 6 and 24 hours were observed MG-63 (Figure 5A-5B). Similarly, the protective effect of the carbon-BNQDs against PB4 (0.15 µM) for all cell lines investigated are depicted in Figures 5C-5D. The MMT assay for Caco-2 treated with PB4 showed a cell viability of 68.7% and 80 % after 6 and 24 hours, respectively. The beneficial effect of the BNQDs on CaCo-2 line was demonstrated by the increase in cell viability value to about 95.2 and 100% after 6 and 24 hours. Similarly, on MG-63 lines treated with PB4 the cell viability increases with BNQD pre-treatment from 93.4% to 106% and from 76% to 95.1% after 6 and 24 hours respectively. Finally, the beneficial effect of the carbon-BNQDs on HMC3 cell line was evident after 6 hours of incubation, when the cell viability increases from 81.1% to 101 % in BNQD-pre-treated cells. No significant toxic effect was observed for PB4 on HMC3 cell at longer incubation time (24h). The values evidencing the significance difference between pretreated and non-pretreated cells are summarized in table S5.

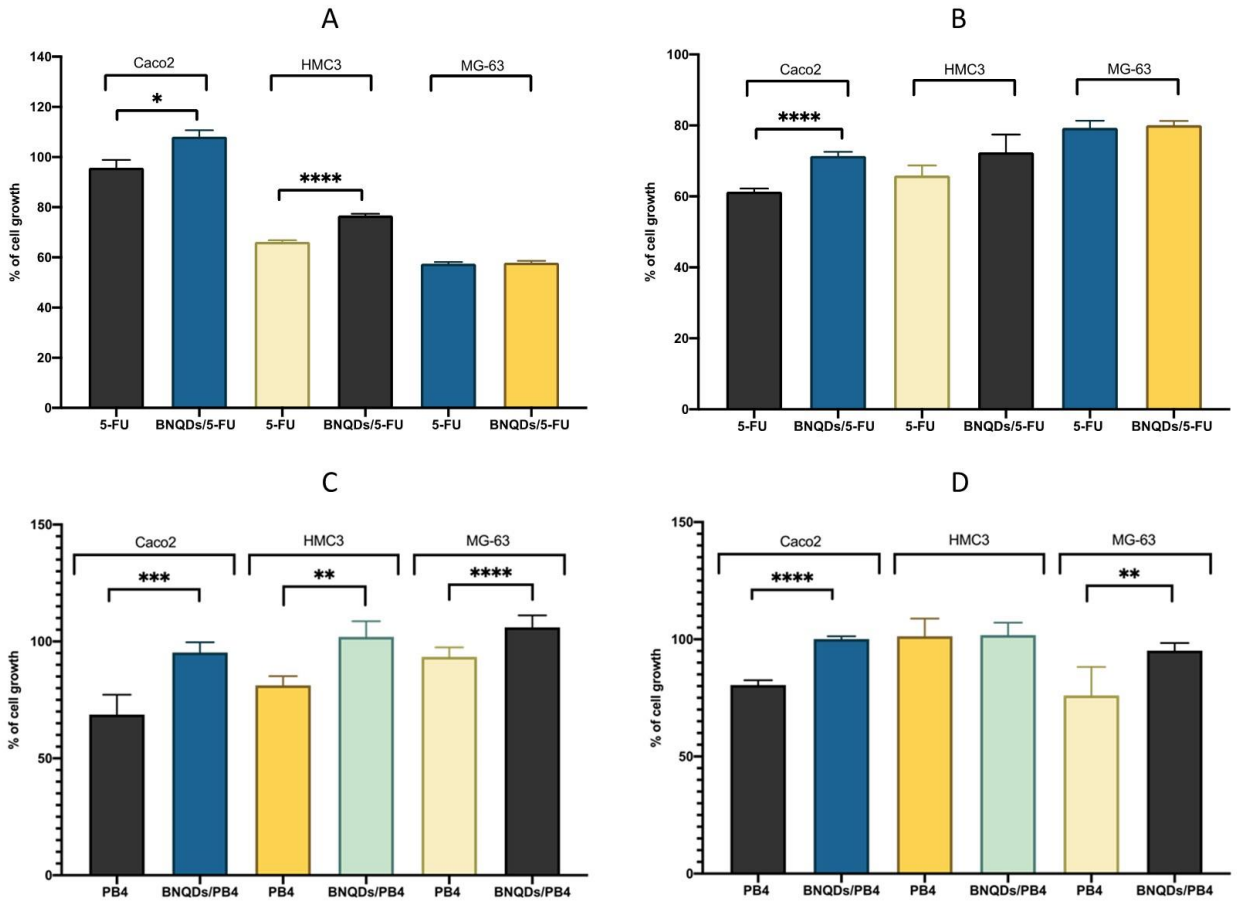

Figure 5. Percentage of cell growth for Caco-2, HMC-3 and MG-63 cell lines compared to control (untreated cells 100 %) after treatments with A) 5-Fu (100 µM) and BNQDs (4 µg 200 μL^{-1}) for 6 hrs; B) 5-FU (100 µM) and BNQDs (4 µg 200 μL^{-1}) for 24 hrs; C) PB4 (0.15 µM) and BNQDs (4 µg 200 μL^{-1}) for 6 hrs; D) PB4 (0.15 µM) and BNQDs (4 µg 200 μL^{-1}) for 24 hrs.

These results show an effective cell protection effect of the phenol-BNQDs (4 µg 200 μL^{-1}) towards the selected toxic agents 5-Fu (100 µM) and PB4 (0.15 µM). Increase of cell viability at both early (6h) and late (24h) incubation time was observed for BNQD-treated Caco-2 and HMC-3 cells insulted with 5-Fu. A higher protective effect of the phenol-BNQDs (100% cell vitality) was observed in Caco-2, HMC-3, and MG-63 cells insulted with PB4.

2.7. RPKM RNA expression evaluation and DEG analysis

To investigate the molecular causes of the beneficial effect of the carbon-BNQDs, we decided to perform gene expression analyses on the three cell lines, Caco-2, MG-63 and HMC-3. Untreated and BNQD-pretreated (20 ng/µL) cells were insulted with PB4 (0.15 µM) at different incubation time (6 and 24 hours). All experiments were consciously conducted with a low amount of toxic agent in order

to induce metabolic changes, detectable by gene expression changes, without cells death. No cell damage was observed after the incubation by optical microscopy investigation. Statistical analysis performed with GraphPad Prism, specifically a 2-way ANOVA test, corrected for multiple comparisons by controlling the False Discovery Rate with a Two-stage step-up method of Benjamini, Krieger and Yekutieli, revealed two statistically significant gene group: **GPX1-GSTP1-PARK7-SOD1-TXN-HMOX1** involved in oxidative stress process[67-71] and **CCL2-CSF3-IL6-IL8-CSF2** and **PTSG2** involved in immunoregulation and inflammation events.[72-75] Modification of the gene expression, especially for oxidative metabolism, was observed for all cell lines investigated upon PB4 exposure. The pre-treatment with the carbon-BNQDs resulted in the total expression recovery of the genes responsible for damage reparation (reaching the CTRL condition 100%) and modification of gene expression involved in oxidative damage protection and inflammation (Table S6-S8).

The pretreatment with carbon-BDQNs decreased the expression of **PARK7** gene, encoding for a redox-sensitive chaperone,[76] and involved in oxidative stress protection and cell death prevention processes. The under expression of this gene is indicative of a low oxidative stress. Therefore, it is probable that the reduced expression of **PARK7** gene in the PB4-insulted Caco-2 cells is related to the capability of the phenol-BNQDs to inactivate ROS products. **SOD1** gene is involved on free superoxide radical removal process and is crucial during the elevated endogenous and exogenous ROS phases promoting the transcription of genes involved on the resistance and reparation processes after the oxidative stress.[77] In Caco-2 and MG-63 cell lines, the BNQDs treatment induced a net increase of **SOD1** gene expression after 24 hours of incubation to suggest an effective BNQDs antioxidant effect. The beneficial effect of the BNQDs was also revealed by the increased expression of the **HMOX1** gene, suppressed by the cytotoxic PB4, in Caco-2 (24h) and HMC-3 (6h) cells. This gene is involved in cellular response to the oxidative stress through the conversion of heme to biliverdin by ferrous iron.[78] **GSTP1** gene encodes the detoxicant enzyme glutathione S-transferase π, which is involved in oxidative stress and damage process from free radicals. In Caco-2 cells after 24 hours from the PB4 exposure an increase of **GSTP1** gene expression was observed to indicate that oxidative stress from radicals occurs. In the presence of the phenol-BNQDs, the GSTP1 expression lowers to reach the normal level (100% of CTRL). This result could suggest the radical scavenger effect of the BNQDs, reasonably due to the phenolic groups.

Two other genes particularly altered after PB4 treatment are **GPX1** and **TXN**. These genes are involved in the metabolism of hydroperoxides and hydrogen peroxide to protect the cells from the oxidative damage. Pretreatment with the phenol-BNQDs enhanced **GPX1** expression at 6 and 24h. **TXN** is a target of NRF2, this gene is part of the response to intracellular nitric oxide and provides a defense against oxidative stress by reducing peroxides species. It also controls intracellular redox

environment, protein reduction/oxidation, cellular growth and apoptosis, and supports peroxiredoxin (PRDX)-mediated H_2O_2 clearance. In PB4-stimulated Caco-2 and HMC3 cells, the pretreatment with phenol-BNQDs reduced **TXN** expression with a consequence of minor necessity of this enzyme, sign of a minor ROS production. The reduction of **TXN** expression is more effective for Caco-2 cells at 6 hours. **CCL2** and **CSF3** are antioxidant and pro-inflammatory response genes, involved in the regulation of interleukins **IL-6** and **IL-8**. In MG-63 cells the expression of these genes, after PB4 exposure, resulted in a complex metabolic response. Over expression of **CSF3** and **IL-6** gene and **CCL2** and **IL-8** gene, indicative of an inflammation response to oxidative stress damage, [79] was observed at early time and at longer incubation time (24 hours), respectively. The pretreatment with the carbon-BNQDs decreased **CCL2** (24h) and **CSF3**, **IL-6** and **IL-8** gene expression in PB4 exposed cells. It is plausible that the carbon-BNQDs as other phenolic compounds are anti-inflammatory mediators that reduce the production or activities of proinflammatory cytokines and block immune cell trafficking into tissues. [80-81] In MG-63 cell line exposed to PB4 for 6 hours, an intense over expression of **CSF2** gene which is involved in the immune and inflammatory cascade responses and in the oxidative stress induced by chemical agents,[82] was observed. The beneficial effect of the BNQDs was confirmed by the completely recovery of the **CSF2** gene expression level. **PTGS2** (prostaglandin-endoperoxide synthase 1) gene expression is involved in the arachidonic acid pathway, the first step of inflammation process. [83-84] The experiment evidenced a decrease of expression gene level in MG-63 cell exposed to PB4 and a completely restore of the expression with the BNQDs treatment at early time.

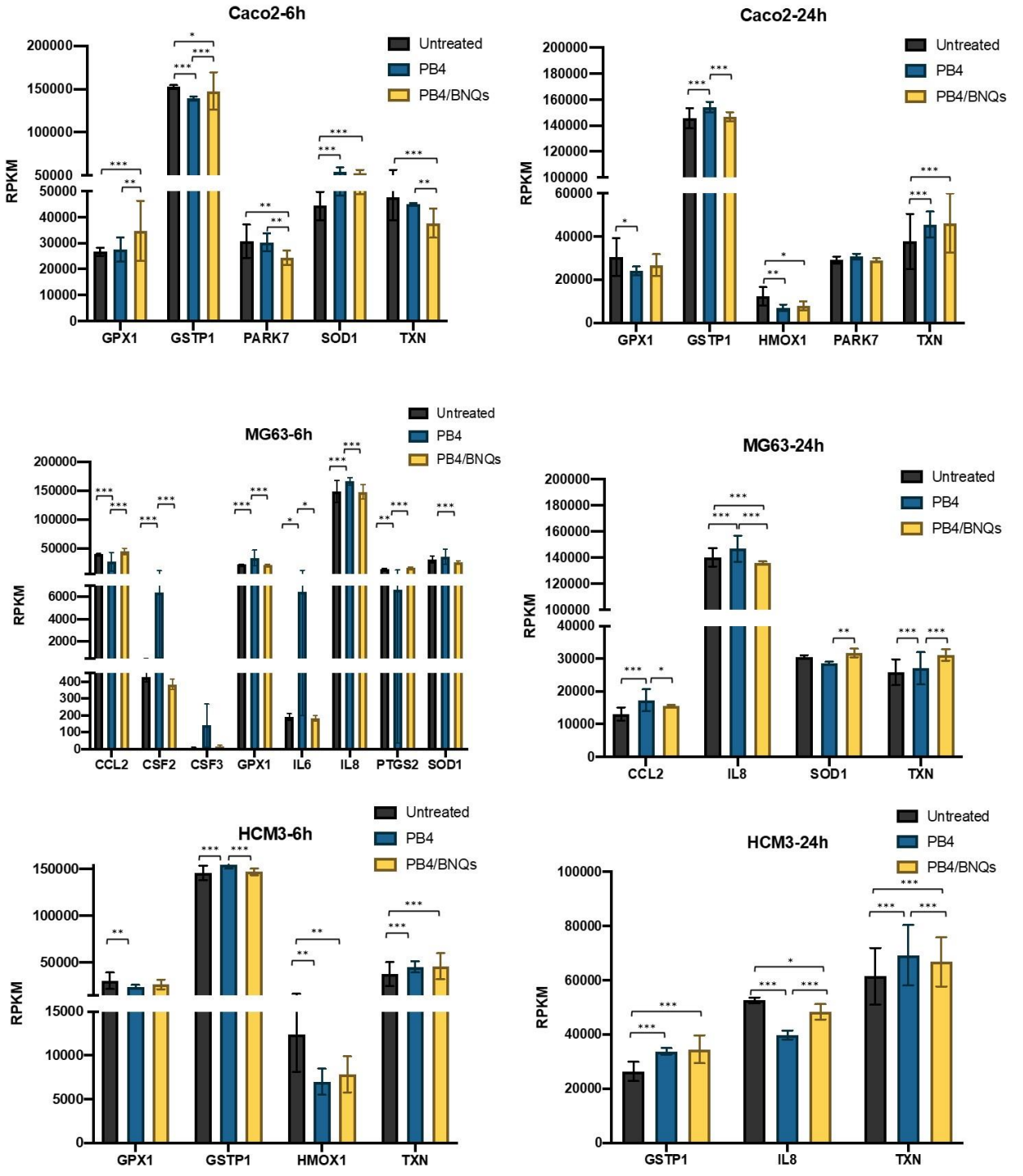

Figure 6. RNA expression evaluation: RPKM values with statistical differences for Caco-2, MG63 and HMC3 cell lines, at 6 and 24 hours. RPKM for untreated cells in black (control), RPKM for cells exposed to PB4 in blue and RPKM for pretreated-BNQD cells in yellow. The 2-way ANOVA test was performed by Benjamini, Krieger and Yekutieli normalization (*p*-values are reported in table S4).

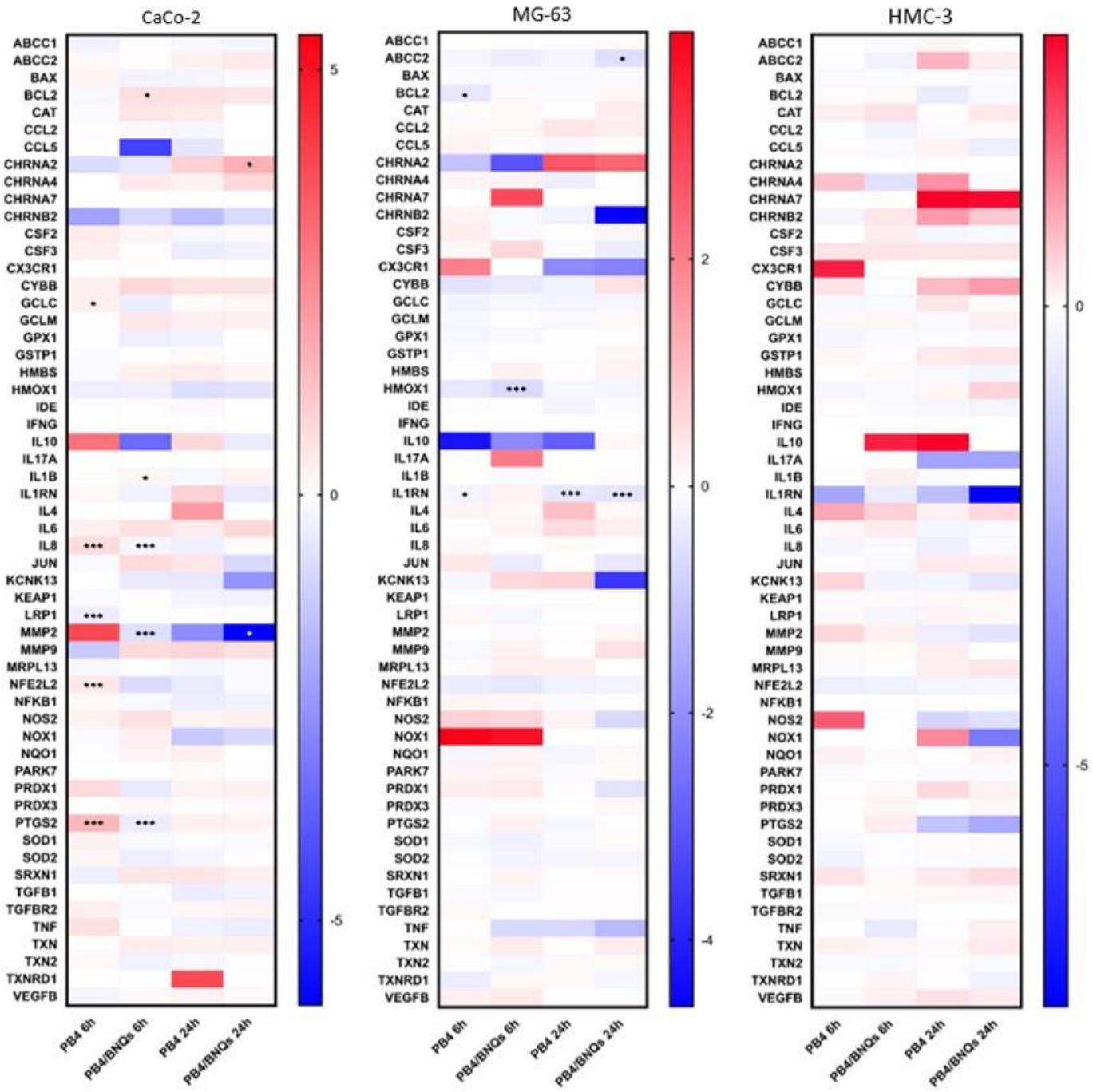

Figure 7. DEG analysis: Heat Maps calculated on the Log_2 Fold Change values for all three cell lines upon PB4 (0.15 µM) exposure without and with BNQDs pretreatment (20 ng/µL) at 6 h and 24h compared to control. The red color stands for an increased expression, while the blue color stands for a reduced expression. * = *p-value <0.05*, ** = *p-value < 0.01*, *** = *p-value < 0.001*.

Figure 7 shows the Heat Maps of Different Expression Gene (DEG) analysis for the three cell lines investigated. It reports the cell metabolic responses to PB4 exposure (at 6 and 24 hour of incubation) in untreated- and BNQDs-pretreated cells. A positive value of log_2 Fold Change indicates an increase of gene expression (red colour), while a negative fold change indicates a decrease in gene expression

(blue colour), both referred to the basal condition at 6 and 24 hours. The experimental results show that Caco-2 cells respond to the PB4 toxic stimulus after 6 hours raising the expression of GCLC, IL8, NFE2L2 and PTGS2 genes. To contrast this toxic stimulus the lower-expression of IL8, PTGS2 and MMP2 genes together with the overexpression of CHRNA2 (after 24 hours) were observed upon BNQDs pretreatment. For MG63 cells the exposure to PB4 induces a lower-expression of BCL2 and IL1RN genes, after 6 and 24 hours. The beneficial effect of the BNQD treatment is ascribable to the down-expression of HMOX1 (after 6 hours), ABCC2 and IL1RN genes (after 24 hours). The DEG experiments showed no statistically significant difference in HMC3 cells. This result highlighted that the cell protection effect of the phenol-BNDQs is more effective in adenocarcinoma and osteosarcoma cells than microglial cells, evidencing a cell line-dependent biological effect. In summary, the RNA-seq data indicate that the protective effect of the phenol-BNQDs in cells insulted with toxic PB4 is related to the expression modification of genes involved in cell protection from both oxidative-stress and inflammation phenomena. As detailed in scheme 1, the antioxidant activity of the phenol-BNQDs induces over-expression of GPX1, SOD1 and HMOX1 genes, involved in damage reparation, and down-expression of GSTP1, PARK7 and TXN genes, due to ROS inactivation. Down-expression of CSF3, IL6, IL8, CCL2 and CSF2 genes and over-expression of PTSG2 gene are instead responsible for the inflammatory damage overcoming.

These results agree with the known antioxidant and anti-inflammatory activity of phenolic compounds. The carbon-BNQDs treatment is a booster that implements the natural cellular response to toxic agents without interference on the metabolic native pathways. This is a key point because carbon-BNQDs could be used in combination with other compounds to support an anti-oxidative therapy.

3. Conclusion

Water dispersible, luminescent and photothermal carbon-BNQDs were produced by a solvent-assisted one-pot synthesis. It is the first example of direct preparation of carbon containing BNQDs, until now only post-synthesis functionalization has been reported. Physicochemical and morphological characterization of the carbon-BNDQs was performed. Detailed investigations proved that the carbon terminations (phenolic, carboxylic and amide groups) on the edge of the carbon-BNQDs can modulate their features such as pH-dependent luminescence, Z-potential and photothermal properties. The carbon-BNDQs possess good biocompatibility and remarkable cell protection effects against toxic agents, proved on human colorectal adenocarcinoma, osteosarcoma and microglial cell lines. Amplicon mRNA-seq analysis for the expression of 56 genes evidenced that

the molecular causes of the carbon-BNQDs beneficial effect are mainly related to protection from oxidative stress, apoptosis, and inflammation. These findings in addition to the demonstrated carbon-BNDQs photothermal properties and the possibility to further functionalize the terminal phenolic and carboxylic groups inspire the use of the carbon-BNQDs in future research aimed to develop novel bioactive low-dimensional materials for applications ranging from electronics to medicine.

4. Experimental section

Materials: All reagents were purchased by Merck (Italy) and used as received. Human colorectal cancer Caco-2 (HTB-37^{TM}, ATCC), microglial HMC-3 (CRL-3304^{TM}), and osteosarcoma MG-63 (CRL-1427^{TM}) cell lines (American Type Culture Collection, 0801 University Blvd, Manassas, Virginia, 20110, United States) were used for biological experiments. 5-Fluoroacil (5-Fu, Ref. F6627) was purchased by Merck (KGaA, Darmstadt, Germany) whereas 2,6-Bis{(E)-2-[4-(Dimethylamino)phenyl]vinyl}-1-methylpyridinium iodide (PB4) was prepared as reported in literature.[63-64]

Preparation of carbon-BNQDs: An amount of 0.152 gr (0.01 mol) of 4-hydroxyphenylboronic acid was dissolved in 5 mL of DMF, after stirring to the resulting solution an amount of 0.12 gr (0.019 mol) of urea was added, then the mixture was heated at 200 °C for 6 hrs. The solvent was evaporated, and the reddish solid product was dispersed in 2 mL of deionized water. The resulting dispersion was purified by dialysis (dialysis membrane 6-8 KDa cut off, MilliQ-water) for 18 hours. The same procedure was used for the reaction in THF refluxed for 6 hrs.

Preparation of bare-BNQDs: An amount of 0.618 gr (0.01 mol) of boric acid was dissolved in 5 mL of DMF, after stirring to the resulting solution an amount of 0.12 gr (0.019 mol) of urea was added and the mixture was heated at 200 °C for 6 hrs. The white solid was separated by centrifugation (13.000 rpm for 5 min) and washed five time with water to eliminate by-products.

Instrumentation: Optical absorption UV-Vis spectra were acquired by a Perkin Elmer 365 spectrophotometer, the PhotoLuminescence (PL) spectra at different excitation wavelengths were measured by a spectrofluorometer Jasco FP-6500. A quartz cuvette with optical length of 10 mm was used.

DLS and Zeta-potential measurements were performed by using a ZetaSizer NanoZS90 (Malvern Instrument, UK), equipped with a 633 nm laser, at the scattering angle of 90° and at 25 °C

temperature. Size and zeta potential of the particles were calculated by using the Stokes-Einstein's equation and the Henry's equation, respectively.

AFM measurements were carried out in soft tapping mode in air using a Bruker FAST-SCAN microscope. The samples were firstly dispersed in solutions, deposited on a freshly mica substrate and then dried under vacuum (10 mbar). The probes used were FastScan A, with a nominal tip radius of 5 nm, spring constant of 18 N/m, and resonance frequency of 1.400 KHz. The scanner was calibrated using a 1 µm x 1 µm reference grid. AFM images were obtained with a tip velocity of 20 µm/s and a target amplitude of about 15 nm. The pixel resolution was fixed at about 1,000 x 1,000 points. Each sample was typically characterized by acquiring five images obtained at different points.

Voltammetric measurements were performed using an VERSTAT potentiostat. All measurements were conducted, using a conventional three electrode system. The screen-printed three-electrodes (SPEs) utilised throughout this work consisted of a gold working electrode, a platinum counter electrode and an Ag/AgCl reference electrode (DROP-sense).

X-ray photoelectron spectroscopy (XPS) spectra of the freshly prepared samples, deposited on Si substrates, were measured at 45° relative to the sample stage plane with a PHI 5600 Multi Technique System (base pressure of the main chamber $1x10^{-8}$ Pa). Spectra were excited with monochromatized Al-Kα radiation. The pass energy was set to 11.85 eV. XPS peak intensities were obtained after Shirley background removal. Spectra calibration was achieved by fixing the Ag $3d_{5/2}$ peak of a clean sample at 368.3 eV; this method turned the C 1s peak of the aliphatic C-C bond at 285.0 eV. Experimental uncertainties in binding energies lie within ± 0.4 eV. The fittings of the XP spectra were carried out using Gaussian envelopes after subtraction of the background until there was the highest possible correlation between the experimental spectrum and the theoretical profile. The residual or agreement factor R, defined by $R = [\Sigma (F_{obs} - F_{calc})^2 / \Sigma (F_{obs})^2]^{1/2}$, after minimization of the function $\Sigma (F_{obs} - F_{calc})^2$, converged to the value of 0.03. The fitting was performed using the XPSPEAK4.1 software. The surface atomic concentration of the samples was calculated considering the relevant atomic sensitivity factors.

Nuclear Magnetic Resonance (^{1}H-NMR) spectra of the lyophilized sample (Lyoquest-85 instrument, Telstar, MI, Italy) were acquired on a Bruker Avance 400 spectrometer at 297 K in D_2O solvent. Chemical shifts (δ) are expressed in parts per million (ppm) and reported relative to the residual water proton peak.

Modelling Simulation. Modelling Simulation. The geometry of the BNQD structures was optimized by Consistent Valence Force Field which encompass potential energy contributions from both bonded interactions (such as bond lengths, bond angles, torsion angles, and out-of-plane interactions) and non-bond interactions. The latter are characterized by the 12–6 Lennard–Jones potential for van der

Waals (VdW) interactions, along with a Coulombic representation for electrostatic interactions. Optimized structures were then fully optimized within the DFT framework employing the hybrid B3LYP functional and the 6-31G basis set augmented with polarization and diffuse functions to simulate neutral and anionic derivatives.[85-88] Optical absorption spectrum simulation was carried out with the TD-DFT approach, using the CAM-B3LYP functional.[89] The polarizable continuum model (PCM) was used to model the solvation effect for neutral and anionic structures, and the lowest 40 energy states were considered in water solvent.[90] All the calculations were performed with the Gaussian 16 package,[91] molecular orbitals (MOs) were displayed by using the Multiwfn 3.8 program.[92]

Raman spectra were excited in a backscattering geometry with a Nd:YAG laser (532 nm) and recorded by a WITec alpha 300 confocal Raman apparatus. The laser radiation was focused on the samples (spot diameter of about 2 μm) at a low laser power to avoid heating and the excitation and scattered radiation were collected using a ZEISS Objective LD EC Epiplan-Neofluar 50× with a numerical aperture 0.25. The integration time for each spectrum was of 10 s. To generate 2D chemical maps, Raman spectral imaging was performed with the same instrument and probing light source. In this case a grid of 10000 spectra with an integration time of 0.02 s was acquired over a sample area of 2500 μm^2.

Fourier Transform Infrared Spectroscopy-Attenuated Total Reflection (FTIR-ATR) measurements were recorded using the FT-IR Imaging System PerkinElmer Frontier Spotlight 400 in the range 4000-550 cm^{-1}, with 4 cm^{-1} resolution and 16 scans. Atmospheric corrections were applied to the background. The sample powders were placed on the ATR crystal by applying a pressure to be adhered completely until the signals became stable.

Biocompatibility of the carbon-BNQDs: To evaluate the effect of the BNQDs, MTT ([3-(4,5-dimethylthiazol-2-yl)-2,5-diphenyltetrazolium bromide]) assay was performed. Briefly, human colorectal adenocarcinoma cells (Caco-2) were grown in Dulbecco's MEM (DMEM, Ref. 10569-010, ThermoFisher Scientific,168 Third Avenue, Waltham, MA USA 02451) with 10% heat-inactivated fetal bovine serum, 2 mM L-Alanyl-L-Glutamine, penicillin-streptomycin (50 units-50 μg/ mL) and incubated at 37 °C in a humidified atmosphere of 5% CO_2, 95% air. Caco-2 cells were plated in 96 well pates and incubated at 37 °C. 4 mg of BNQDs were dispersed in 40 μL of nuclease free water (0.1 mg/μL) and serial dilutions were obtained: 1 μg/μL, 100 ng/μL, and 10 ng/μL, and 1 ng/μL. Cells were treated with 40 μL of each solution. 5-Fluoroacil (5-Fu) was prepared as a 1 mM solution in 10 mL water with 0.01% DMSO and tested at concentrations of 100 μM, 10 μM, 1 μM, 0.1 μM and 0.01 μM. Untreated cells were used as controls. Microplates were incubated at 37 °C in

a humidified atmosphere of 5% CO_2, 95% air for 24 h. Cytotoxicity of 5-FU was measured by a colorimetric assay based on the use of tetrazolium salt MTT (3-(4,5-dimethylthiazol-2-yl)-2,5-diphenyl tetrazolium bromide, Ref. M6494, ThermoFisher Scientific,168 Third Avenue, Waltham, MA USA 02451) and calculating growth inhibition relative to untreated controls. The results were read on a BioTek Synergy H1 Multimode Reader (Agilent, 5301 Stevens Creek Blvd, Santa Clara, CA 9505, United States) using a wavelength of 569 nm. Each value was an average of 8 wells, always using the MTT assay and based on the difference in absorbance by the wells treated with -BNQDs (Figure 4). All statistical analyses were performed using GraphPad Prism 8.0 software (GraphPad Software, San Diego, California USA, www.graphpad.com).

Evaluation of the Protective Effect of the carbon-BNQDs from 5-Fluorouracil and Heteroaryl-Ethylene insult: The protective effect of BNQDs from exogenous compounds 5-Fluorouracil (5-Fu) and 2,6-Bis{(E)-2-[4-(Dimethylamino)phenyl]vinyl}-1-methylpyridinium iodide (PB4)[66, 93] was evaluated in three cell lines: colorectal adenocarcinoma (Caco-2 HTB-37^{TM}), osteosarcoma (MG-63 CRL-1427^{TM}) and microglial (HMC-3 CRL-3304^{TM}) cells. Caco-2 were grown as described in the previous section, while MG-63 and HMC-3 cells were grown in minimum essential medium (MEM, Ref. 42360-024, ThermoFisher Scientific,168 Third Avenue, Waltham, MA USA 02451) with 10% heat-inactivated fetal bovine serum, 2 mM L-Alanyl-L-Glutamine, penicillin-streptomycin (50 units-50 μg/mL) and incubated at 37 °C in a humidified atmosphere of 5% CO_2, 95% air. After 24 hours of plating, cells were treated with BNQDs (20 ng/μl). Untreated cells were used as control. After 24 hours of incubation, the cytotoxic was simulated at both conditions using 5-FU (100 μM) and PB4 0.15 μM. The effect on the three cell lines was evaluated with a MTT assay performed as previously described at 6 and 24 hours.

Cell treatment with carbon-BNQDs *and RNA extraction for RNA-seq experiment:* To evaluate the biological activity of the BNQDs, the same cell lines mentioned above were treated under the following conditions: i) with PB4 (0.15 μM) for 6 and 24 hours, ii) pre-treated with BNQDs (20 ng/μL) for 24h, washed with PBS 1X and then insulted with PB4 for 6 and 24 hours. Untreated cells were used as controls. All treatments were carried out in triplicate. After 6 or 24 hours, the cells were resuspended in a mixture of b RLT buffer supplied with RNeasy Mini Kit (QIAGEN, Darmstadt, Germany) with 1% β-mercaptoethanol. Then RNA extraction was carried out according to the instructions provided in the RNeasy Mini Kit and the extracted RNA was quantified with the Qubit RNA HS Assay Kit (Ref. Q32852, ThermoFisher Scientific,168 Third Avenue, Waltham, MA USA 02451) on a Qubit 4 Fluorometer instrument (Ref. Q33238, ThermoFisher Scientific,168 Third

Avenue, Waltham, MA USA 02451). Further quantification was performed with an RNA Integrity Number Assay (RIN) using Agilent RNA 6000 Nano Kit (Ref. 5067-1511, Agilent, 5301 Stevens Creek Blvd, Santa Clara, CA 9505, United States) on a 2100 Bioanalyzer instrument (Ref. G2939BA, Agilent, 5301 Stevens Creek Blvd, Santa Clara, CA 9505, United States). The results of the quantifications are shown in Table S7. The values are the arithmetic mean of the triplicates.

Libraries preparation and sequencing: The libraries have been prepared following the manufacturer's instructions provided by the protocol generated by the website https://support.illumina.com/custom-protocol-selector.html. The Sequencing Instrument was MiSeq with MiSeq Reagent Kit v3. the library preparation Kit used was AmpliSeq for Illumina Custom and Community Panels, a dual indexing. The RNA input used was 100 ng for all samples, calculated considering the Qubit quantification, as the manufacturer instructions. Each sample was processed as triplicate. The preparation was carried out by the AmpliSeq TM cDNA Synthesis for Illumina kit (Ref. 20022654, Illumina Inc., San Diego, California, USA) for retrotranscription, the AmpliSeq TM Library PLUS for Illumina (Cat. 20019102, Illumina® Inc., San Diego, California, USA) for preparation and the AmpliSeq TM CD Indexes, Set A for Illumina® (96 Indexes, 96 Samples) (Ref. 20019105, Illumina® Inc., San Diego, California, USA) for sample indexing. The custom panel was designed using the Illumina DesignStudio Assay Design Tool (Illumina® Inc., San Diego, California, USA). This provided the sequencing of 56 genes (Table S8). Denaturing and dilution of libraries were performed following the "Denature and Dilute Libraries Guide" protocol provided by Illumina® (Document # 15039740 v10). Finally, sequencing was performed using the MiSeq Reagent Kits v3 (Ref. 15043895, Illumina® Inc., San Diego, California, USA) on a MiSeq Instrument (Cat. SY-410-1003, Illumina® Inc., San Diego, California, USA).

Bioinformatic analysis and RNA expression evaluation: Sample sheet for the sequencing was created with Illumina Experiment Manager software (Illumina® Inc., San Diego, California, USA) and selecting a FASTQ workflow. This performs a demultiplexing step for runs with index reads and multiple samples. After demultiplexing, the workflow generates analysis output in the FASTQ file format. The FASTQ files are suitable for secondary analysis using third-party analysis tools. FASTQ files processing, Bioinformatic analysis and Different Expression Gene[1,2] were carried out using QIAGEN CLC Genomics Workbench v. 21 (QIAGEN, Hilden, Germany). Different Expression Gene is a CLC tool that declares a gene as differentially expressed if there is a difference or change observed in read counts or expression levels/index between two experimental conditions. Statistical

analysis was performed using GraphPad Prism version 8.0.0 for Windows (GraphPad Software, San Diego, California USA, www.graphpad.com). To evaluate gene expression and its variations in various genes, Heat Maps were built on GraphPad using Fold Change values generated by CLC. A statistical analysis was conducted using the values of Reads Per Kilobase of exon model per Million mapped reads (RPKM) obtained on CLC[3]. On these values a 2-way ANOVA test was performed on GraphPad Prism, used to estimate how the mean of a quantitative variable (in this case the RPKM) changes according to the levels of two categorical variables. This test was additionally corrected for multiple comparisons by controlling the False Discovery Rate with a two-stage step-up method of Benjamini, Krieger and Yekutieli[4].

Supporting Information

Supporting Information is available from the Wiley Online Library or from the authors.

Figure S1. Optical absorption spectra during BNQDs formation in DMF. **Figure S2.** Optical absorption spectra of BNQDs preparation in THF. **Figure S3.** Optical absorption spectrum of bare-BN water dispersion. **Figure S4.** FTIR-ATR spectra of urea and boron precursor. **Figure S5.** Raman patterns for bare-BN and BNQDs. **Figure S6.** Aromatic region of the-2D-NMR COSY spectrum of BNQDs. **Figure S7.** Methyl region of the ^{1}H NMR spectrum of urea in DMF at 200 °C for 6 h. **Figure S8.** ^{1}H-NMR spectra of urea and (4-hydroxyphenyl)boronic acid in THF at 200 °C for 6 h and (4-hydroxyphenyl)boronic acid. **Figure S9.** Aromatic region of the ^{1}H NMR spectra of urea and (4-hydroxyphenyl)boronic acid in DMF at 200 °C. **Figure S10.** Representative AFM images of BNQDs on MICA substrate. **Figure S11.** Cyclic Voltammograms for boron-precursor and BNQD dispersion. **Figure S12.** Cyclic Voltammograms for BNQD dispersion. **Figure S13.** Plot of BNQD Ea peak at various pH. **Figure S14.** HOMO-LUMO molecular orbitals shape for the structures: BNQDsH, BNQDsOH and BNQDs. **Figure S15.** BNQDs PL intensity measurements during three pH-cycles. **Figure S16.** Photothermal time constant (τ_s) calculation for BNQDs. **Figure S17.** Photothermal time constant (τ_s) calculation for BNQDs-agarose 0.4%. Photothermal measurements. Figure S18. Optical absorption spectra for different amount of carbon-BNQDs dispersion in water.. **Scheme S1.** Redox mechanism of *para*-substituted phenols. **Table S1**. XPS Atomic Concentration Analysis (%) and Binding Energies (eV). **Table S2.** Photothermal conversion efficiency (η) of BNQDs. **Table S3.** Photothermal conversion efficiency (η) of BNQD/agarose 0.4%. **Table S4.** Statistical analysis with Dunnett's Multiple comparisons with two different references: all condition vs 5-Fu; all condition vs control. **Table S5.** Quantification performed after RNA extraction on all cell treatment conditions.

Table S6. Statistical analysis comparisons of pretreated cells and not pretreated cells after cytotoxic impact with PB4. **Table S7**. Quantification performed after RNA extraction on all cell treatment conditions. **Table S8.** Genes in the RNAseq panel. Photothermal measurements.

Corresponding Authors

Give contact information for the author(s) to whom correspondence should be addressed.

*Salvatore Petralia salvatore.petralia@unict.it; *Nicolò Musso: nmusso@unict.it

Author Contributions

The manuscript was written through contributions of all authors. All authors have given approval to the final version of the manuscript.

ACKNOWLEDGMENTS

This work has been funded by European Union (NextGeneration EU), through the MUR-PNRR project SAMOTHRACE (ECS00000022) and MUR ex D.M.n.1059 del 09/08/2021 (CUP: E93C22003310001) Project title: L'innovazione delle Biotecnologie nell'Era della Medicina di Precisione, dei Cambiamenti climatici e dell'Economia Circolare.

G.M.L. Consoli: investigation and writing original manuscript, L. Maugeri: investigation, N.Musso: investigation, A. Gulino:investigation, L. D'Urso:investigation, P. Bonacci: investigation, G. Buscarino: investigation, G. Forte:investigation, and S. Petralia: supervisor, investigation, funding resource and writing original manuscript

The authors gratefully acknowledge the PON project Bionanotech Research and Innovation Tower (BRIT) for the technical assistance and use of laboratories. Mr. G.F. Indelli is acknowledged for the technical support.

Conflict of Interest

The authors declare no competing financial interest.

Data Availability Statement

The data that support the findings of this study are available from the corresponding author upon reasonable request.

References

[1] C. Wu, X. Zhang, R. Wang, L. J. Chen, M. Nie, Z. Zhang, X., Huang, L. Han. *Nanotechnology* **2022**, *33*, 072001.

[2] H. Rahman, H. Md. Rossain, T. Ferdous. *J. Mol. Liq.* **2020**, *320*, 114427.

[3] A. A. H. Abdellatif, M. A. Younis, M. Alsharidah, O. Al Rugaie, H. M. Tawfeek. *Int. J. Nanomed*. **2022**, *17*, 1951.

[4] A. A. Yaqoob, H. Ahmad, T. Parveen, A. Ahmad, M. Oves, I. M. I. Ismail, H. A. Qari, K. Umar, M. Ibrahim. *Front. Chem*. **2020**, *8*, 341.

[5] Y. Yoon, P. L. Truong, D. Lee, S. H. Ko. *ACS Nanosci. Au* **2022**, *2*(2), 64.

[6] G. Li, Z. Liu, W. Gao, B. Tang. *Coord. Chem. Rev.* **2023**, *478*, 214966.

[7] P. M. Revabhai, T. J. Park, S. K. Kailasa. *Inorg. Chem. Commun.* **2023**, *148*, 110346.

[8] S.Y. Lim, W. Shen, Z. Gao. *Chem. Soc. Rev.* **2015**, *44*, 362.

[9] L. Maugeri, G. Forte, M. A. Messina, M. Camarda, G. Ventimiglia, G. M. L. Consoli, S. Petralia. *ACS Appl. Nano Mater.* **2022**, *5* (8), 10167.

[10] G. M. L. Consoli, G. Forte, L. Maugeri, V. Consoli, V. Sorrenti, L. Vanella, G. Buscarino, S. Agnello, M. Camarda, G. Granata, L. Ferreri, S. Petralia. *ACS Appl. Nano Mater*. **2023**, *6*, 358.

[11] G. M. L. Consoli, M. L. Giuffrida, C. Satriano, T. Musumeci, G. Forte, S. Petralia. *Chem. Commun*. **2022**, *58*(19), 3126.

[12] G. M. L. Consoli, M. L. Giuffrida, S. Zimbone, L. Ferreri, L. Maugeri, M. Palmieri, C. Satriano, G. Forte, S. Petralia. *ACS Appl. Mater. Interfaces* **2023**, *15*, 5732.

[13] S. Angizi, A. A. A. Sayed, M. H. Azar, F. Shayeganfar, M. I. Manning, A. Hatamie, A. Pakdel, A. Simchi. *Prog. Mater. Sci.* **2022**, *124*, 100884.

[14] A. Acharya, S. Sharma, X. Liu, D. Zhang, Y. K. Yap. *J. Carbon Res*. **2021**, *7*, 35.

[15] B. Huo, B. Liu, T. Chen, L. Cui, G. Xu, M. Liu, J. Liu. *Langmuir* **2017**, *33*, 10673.

[16] Z. Lei, S. Xu, J. Wan, P. Wu. *Nanoscale* **2015**, *7*, 18902.

[17] S. Y. Lim, W. Shen, Z. Gao. *Chem. Soc. Rev*. **2015**, *44*, 362.

[18] B.-P. Qi, H. Hu, L. Bao, Z.-L Zhang, B. Tang, Y. Peng, B.-S. Wang, D.-W. Pang. *Nanoscale* **2015**, *7*, 5969.

[19] L. B. Drissi, H. Ouarrad, F. Z. Ramadana, W. Fritzsch. *RSC Adv.* **2020**, *10*, 801.

[20] H. Ouarrad, F. Z. Ramadan,L. B. Drissi. *Optic. Express* **2020**, *28* (24), 36656.

[21] Q. Weng, X. Wang, X. Wang, Y. Bando, D. Golberg. *Chem. Soc. Rev.* **2016**, *45*, 3989.

[22] S. Angizi, F. Shayeganfarc, M. H. Azara, A. Simchia. *Ceram. Int.* **2020**, *46*, 978.

[23] Y. Ding, P. He, S. Li, B. Chang, S. Zhang, Z. Wang, J. Chen, J. Yu, S. Wu, H. Zeng, L. Tao. *ACS Nano* **2021**, *15*, 14610.

[24] Y. C. Boo. *Antioxidants* **2019**, *8*, 379.

[25] E. Huarte, C. Cid, A. Azqueta, M.-P. De Pena. *Eur. J. Nutr*. **2021**, *60*, 677.

[26] S. Li, S. Yin, H. Ding, Y. Shao, S. Zhou, W. Pu, L. Han, T. Wang, H. Yu. *Cell Prolif.* **2023**, *56*, e13346.

[27] A. Lobiuc, N. Pavăl, I. I. Mangalagiu, R. Gheorghiță, G.-C. Teliban, D. Amăriucăi-Mantu, V. Stoleru. *Molecules* **2023**, *28*, 1114.

[28] G. Scapagnini, S. Vasto, N. G. Abraham, C. Caruso, D. Zella, G. Fabio, *Mol. Neurobiol*. **2011**, *44*, 192.

[29] K. B. Pandey, S. I. Rizvi. *Oxid. Med. Cell. Longev*. **2009**, *2*, 270.

[30] T. Hussain, B. Tan, Y. Yin, F. Blachier, M. C. Tossou, N. Rahu. *Oxid. Med. Cell. Longev*. **2016**, 7432797.

[31] Y. Guo, Q. Sun, F.-G. Wu, Y. Dai, X. Chen. *Adv. Mater*. **2021**, *33*, 2007356.

[32] Y. Dai, Z. Yang, S. Cheng, Z. Wang, R. Zhang, G. Zhu, Z. Wang, B. C. Yung, R. Tian, O. Jacobson, C. Xu, Q. Ni, J. Song, X. Sun, G. Niu, X. Chen. *Adv. Mater*. **2018**, *30*, 1704877.

[33] Y. Guo, X. Zhang, W. Sun, H. R. Jia, Y. X. Zhu, X. Zhang, N. Zhou, F. G. Wu. *Chem. Mater.* **2019**, *31*, 10071.

[34] Y. Wang, F. Liu, N. Yan, S. Sheng, C. Xu, H. Tian, X. *ACS Bio-mater. Sci. Eng*. **2019**, *5*, 4700.

[35] W. Shen, Q. Wang, Y. Shen, X. Gao, L. Li, Y. Yan, H. Wang, Y. Cheng. *ACS Cent. Sci.* **2018**, *4*, 1326.

[36] J. Guo, Y. Ping, H. Ejima, K. Alt, M. Meissner, J. J. Richardson, Y. Yan, K. Peter, D. von Elverfeldt, C. E. Hagemeyer, F. Caruso. *Angew. Chem., Int. Ed*. **2014**, *53*, 5546.

[37] Z. Hanif, K.-I. Choi, J.-H. Jung, A. Gesselle, M. Pornea, E. Park, J. Cha, H.-R. Kim, J.-H. Choi, J. Kim. *Ind. Eng. Chem. Res*. **2023**, *62*, 2662.

[38] G. Cassabois, P. Valvin, B. Gil. *Nat. Photon.* **2016**, *10*, 262.

[39] W. Xie, T. Yanase, T. Nagahama, T. Shimada. *J. Carbon Res*. **2016**, *2*, 2.

[40] A. Sunny, A. Balapure, R. Ganesan, R. Thamankar. *ACS Omega* **2022**, *7*, 33926.

[41] F. Shayeganfar, M. R. R. Tabar, A. Simchi, J. Beheshtian. *Phys. Rev. B* **2017**, *96*, 165307.

[42] V. Nguyen, L. Yan, N. Zhao, N. Van Canh, N. T. Nhat Hang, P. H. Le. *J. Mol. Struct.* **2021**, *1244*, 130922.

[43] A. Sunny, A. Balapure, R.Ganesan, R.Thamankar. *ACS Omega* **2022**, *7*, 33926.

[44] T A. Enache, A. M. Oliveira-Brett. *J. Electroanal. Chem.* **2011**, *655*, 9.

[45] Gulino. A. *Anal. Bioanal. Chem*. **2013**, *405*, 1479.

[46] A. Acharya, S. Sharma, X. Liu, D. Zhang, Y. K. Yap. A Review on van der Waals Boron Nitride Quantum Dots. *C* **2021**, *7*, 35.

[47] S. Li, H. Zhang, Z. Liu, J. Xu, G. Fan, W. Li, Q. Li, X. Hu, G. Jing. *Appl. Sci.* **2022**, *12*, 1245.

[48] A. Gulino, G. G. Condorelli, P. Mineo, I. Fragalà. *Nanotechnology* **2005**, *16*, 2170.

[49] A. Gulino, F. Lupo, G. G. Condorelli, P. Mineo, I. Fragalà. *Chem. Mater*. **2007**, *19*, 5102.

[50] A. Pilli, J. Jones, N. Chugh, J. Kelber, F. Pasquale, A. LaVoie. *J. Vac. Sci. Technol. A* **2019**, *37*, 041505.

[51] J. Qu, Q. Li,C. Luo, J. Cheng, X. Hou. *Coatings* **2018**, *8*, 214.

[52] P. K. Rastogi, K. R. Sahoo, P. Thakur, R. Sharma, S. Bawari, R. Podila, T. N. Narayanan. *Phys. Chem. Chem. Phys*. **2019**, *21*, 3942.

[53] N. Graf, E. Yegen, T. Gross, A. Lippitz, W. Weigel, S. Krakert, A. Terfort, W. E. S. Unger. *Surface Sci*. **2009**, *603*, 2849.

[54] A. Gulino, F. Lupo, G. G. Condorelli, M. E. Amato, M. E. Fragalà, G. Scarlata. *J. Mater. Chem*. **2008**, *18*, 5011.

[55] L. Motiei, M. Altman, T. Gupta, F. Lupo, A. Gulino, G. Evmenenko, P. Dutta, M. E. van der Boom. *J. Am. Chem. Soc*. **2008**, *130* (28), 8913.

[56] A. Gulino, P. Dapporto, P. Rossi, I. Fragalà. *Chem. Mater*. **2002**, *14*, 4955.

[57] M. M. Heravi, M. Ghavidela, L. Mohammadkhani. *RSC Adv.* **2018**, *8*, 27832.

[58] M. A. C. Brett, A. M. O. Brett. Cyclic voltammetry and linear sweep techniques, in: Electrochemistry. Principles, Methods and Applications, Oxford University Press, UK, 1993, 174–198.

[59] Q. Weng, X. Wang, X. Wang, Y. Bando, D. Golberg. *Chem. Soc. Rev*. **2016**, *45*, 3989.

[60] P. Gevko, L. Bulusheva, A. Okotrub, V. Koroteev, I. Yushina, L. Bresson, A. Loiseau. *Phys. Stat. Sol.* (b) **2008**, *245*, 2107.

[61] S. Blondy, V. David, M. Verdier, M. Mathonnet, A. Perraud, N. Christou. *Cancer Sci*. **2020**, *111*(9), 3142.

[60] C. Focaccetti, A. Bruno, E. Magnani, D. Bartolini, E. Principi, K. Dallaglio, E. O. Bucci, G. Finzi, F. Sessa, D. M. Noonan, A. Albini. *PLoS One* **2015**, *10*(2), e0115686.

[61] D. Li, C. Song, J. Zhang, X. Zhao. *Toxicology* **2022**, *468*, 153113.

[62] S. Ghafouri-Fard, A. Abak, F. T. Anamag, H. Shoorei, S. A. Javadinia, A. Basiri, M. Taheri. *Front. Oncol*. **2021**, *11*, 658636.

[63] C. Bonomo, P. G. Bonacci, D. A. Bivona, A. Mirabile, D. Bongiorno, E. Nicitra, A. Marino, C. Bonaccorso, G. Consiglio, C. G. Fortuna, S. Stefani, N. Musso. *Antibiotics* **2023**, *12*, 1308.

[64] D. Bongiorno, N. Musso, P. G. Bonacci, D. A. Bivona, M. Massimino, S. Stracquadanio, C. Bonaccorso, C. G. Fortuna, S. Stefani. *Antibiotics* **2021**, *10*, 1034.

[65] Y. Zhao, H. Wang, J. Zhou, Q. Shao. *Cancers* **2022**, *14*, 2560.

[66] T. Li, X. P. Zhao, L. Y. Wang, S. Gao, J. Zhao, Y.-C. Fan, K. Wang. *Int. J. Med. Sci*. **2013**, *10*, 683.

[67] F. Zhang W. Peng, J. Zhang, L. WangL, W. Dong, Y. Zheng, Z. Wang, Z. Xie, T. Wang, C. Wang, Y. Yan. *J. Cell Biochem.* **2021**, *122*, 222.

[68] J. Xu, X. Su, S. K. Burley, X. F. S. Zheng. *Antioxidants* **2022**, *11*, 427.

[69] S. Baig, E. P. Rizi, C. Chia, M. Shabeer, N. Aung, T. P. Loh, F. Magkos, A. Vidal-Puig, R. C. S. Seet, C. M. Khoo, S.-A. Toh. *Front. Endocrinol*. **2019**, *10*, 256.

[70] J. Jin J, J. Lin, A. Xu, J. Lou1, C. Qian, X. Li, Y. Wang, W. Yu, H. Tao. *Front. Oncol*. **2021**, *11*, 722916.

[71] I. Karagiannidis, S. J. Jerman, D. Jacenik, I. Karagiannidis, S. J. Jerman, D. Jacenik, B. B. Phinney, R. Yao, E. R. Prossnitz, E. J. Beswick. *Front Immunol.* **2020**, *11*, 1885.

[72] S. A. Rawlings, S. Heldt, J. Prattes, S. Eigl, J. D. Jenks, H. Flick, J. Rabensteiner, F. Prüller, A. Wölfler, P. Neumeister, H. Strohmaier, R. Krause, M. Hoenigl. *Front Immunol.* **2019**, *10*, 1798.

[73] A. Haghighitalab, M. M. Matin, A. Amin, S. Minaee, H. R. Bidkhori, T. R. Doeppner, A. R. Bahrami. *Sci Rep.* **2021**, *11*, 7825.

[74] I. P. Heremans, F. Caligiore, I. Gerin, G. T. Bommer. *Proc. Natl. Acad. Sci. USA* **2022**, *119*, e2111338119.

[75] C. K. Tsang, Y. Liu, J. Thomas, Y. Zhang, X. F. Zheng. *Nat. Commun.* **2014**, *5*, 3446.

[76] M. Pylväs, U. Puistola, S. Kauppila, Y. Soini, P. Karihtala. *Eur. J. Cancer.* **2010**, *46*(9),1661.

[77] N. Musso, G. Caruso, D. Bongiorno, M. Grasso, D. A. Bivona, F. Campanile, F. Caraci, S. Stefani. *Biomolecules* **2021**, *11*, 72.

[78] S. Hussain, S. Boland, A. Baeza-Squiban, R. Hamel, L. C. J. Thomassen, J. A. Martens, M. A. Billon-Galland, J. Fleury-Feith, F. Moisan, J.-C. Pairon, F. Marano. *Toxicology* **2009**, *260*, 142.

[79] A. Kumar, L. Shalmanova, A. Hammad, S. E. Christmas. *Transpl. Immunol*. **2016**, *35*, 40.

[80] I. P. Pratomo, A. Tedjo, D. R. Noor, Rosmalena. *Int. J. Inflam*. **2023**, 4251299.

[81] T. Wu, H. Wu, J. Wang, J. Wang *J. Neuroinflammation* **2011**, *8*, 22.

[82] W. Qiu, X. Zhang, X. Pang, J. Huang, S. Zhou, R. Wang, Z. Tang, R. Su. *Food Chem. Toxicol*. **2022**, *170*, 113468.

[83] P. Dauber-Osgurthorpe, V. A. Roberts, D. J. Osgurthorpe, J. Woff, M. Genest, A. T. Hagler, *Struct. Funct. Genet*. **1988**, *4*, 31.

[84] A. T. Hagler, S. Lifson, P. Dauber. *J. Am. Chem. Soc.* **1979**, *101*, 5122.

[85] A. D. Becke. *J. Chem. Phys.* **1993**, *98* (2), 1372.

[86] C. Sgarlata, L. D'Urso, G. Consiglio, G. Grasso, C. Satriano, G. Forte. *Comput. And Theor. Chem*. ***2016***, *1096, 1-6*,

[87] T. Yanai, D. P. Tew, N. C. Handy. *Chem. Phys. Lett*. **2004**, *393*, 51.

[88] J. Tomasi, B. Mennucci, R. Cammi. *Chem. Rev*. **2005**, *105* (8), 2999.

[89] M. J. Frisch, , G. W. Trucks, H. B. Schlegel, G. E. Scuseria, M. A. Robb, J. R. Cheeseman, G. Scalmani, V. Barone, G. A. Petersson, H. Nakatsuji, X. Li, M. Caricato, A. V. Marenich, J. Bloino, B. G. Janesko, R. Gomperts, B. Mennucci, H. P. Hratchian, J. V. Ortiz, A. F. Izmaylov, J. L. Sonnenberg, D. Williams-Young, F. Ding, F. Lipparini, F. Egidi, J. Goings, B. Peng, A. Petrone, T. Henderson, D. Ranasinghe, V. G. Zakrzewski, J. Gao, N. Rega, G. Zheng, W. Liang, M. Hada, M. Ehara, K. Toyota, R. Fukuda, J. Hasegawa, M. Ishida, T. Nakajima, Y. Honda, O. Kitao, H. Nakai, T. Vreven, K. Throssell, J. A. Montgomery, Jr., J. E. Peralta, F. Ogliaro, M. J. Bearpark, J. J. Heyd, E. N. Brothers, K. N. Kudin, V. N. Staroverov, T. A. Keith, R. Kobayashi, J. Normand, K. Raghavachari, A. P. Rendell, J. C. Burant, S. S. Iyengar, J. Tomasi, M. Cossi, J. M. Millam, M. Klene, C. Adamo, R. Cammi, J. W. Ochterski, R. L. Martin, K. Morokuma, O. Farkas, J. B. Foresman, D. J. Fox. Gaussian, Inc., Wallingford CT, 2016. Gaussian 16 Rev C.01

[90] T. Lu, F. Chen. Multiwfn: A multifunctional wavefunction analyzer. *J. Comput. Chem*. **2012**, *33*, 580.

[91] P. G. Bonacci, G. Caruso, G. Scandura, C. Pandino, A. Romano, G. I. Russo, R. Pethig, M. Camarda, N. Musso. *Transl. Oncol.* **2023**, *28*, 101599.